Research Square

Preprints are preliminary reports that have not undergone peer review.
They should not be considered conclusive, used to inform clinical practice,
or referenced by the media as validated information.

Ocean-sourced CO2 Boosts Radiolytic Oxidants at Europa's Chaos

Ujjwal Raut

uraut@swri.edu

Southwest Research Institute https://orcid.org/0000-0002-6036-1575

Benjamin Teolis

Southwest Research Institute

Tom Nordheim

Johns Hopkins Applied Physics Laboratory

Silvia Protopapa

Southwest Research Institute https://orcid.org/0000-0001-8541-8550

Bereket Mamo

University of Texas at San Antonio https://orcid.org/0000-0001-6246-2540

Trevor Erwin

Purdue University

Ian Wong

STScI https://orcid.org/0000-0001-9665-8429

Joshua Kammer

Southwest Research Institute

Kurt Retherford

Southwest Research Institute, San Antonio, TX, USA https://orcid.org/0000-0001-9470-150X

Richard Cartwright

Johns Hopkins University Applied Physics Laboratory https://orcid.org/0000-0002-6886-6009

Ty Peterson

The University of Texas at San Antonio

Geronimo Villanueva

NASA Goddard Space Flight Center

Steven Vance

Jet Propulsion Laboratory, California Institute of Technology https://orcid.org/0000-0002-4242-3293

Article

Keywords:

Posted Date: November 2nd, 2026

DOI: https://doi.org/10.21203/rs.3.rs-11485096/v1

License: This work is licensed under a Creative Commons Attribution 4.0 International License.
Read Full License

Additional Declarations: There is **NO** Competing Interest.

Ocean-sourced CO_2 Boosts Radiolytic Oxidants at Europa's Chaos

U. Raut[1,2*], B.D. Teolis[1,2], T.A. Nordheim[3], S. Protopapa[4], B.D. Mamo[2,1], T.P. Erwin[5], I. Wong[6], J.A. Kammer[1], K.D. Retherford[1,2], R.J. Cartwright[3], T. Peterson[2,1], G. Villanueva[7], S. D. Vance[8]

[1*]Center for Laboratory Astrophysics and Space Science Experiments (CLASSE), Space Science Division, Southwest Research Institute, San Antonio, TX, 78238.
[2]Department of Physics and Astronomy, The University of Texas at San Antonio, San Antonio, TX, 78249.
[3]Johns Hopkins Applied Physics Laboratory, Laurel, MD, 20723.
[4]Solar System Science and Exploration Division, Southwest Research Institute, Boulder, CO, 80302.
[5]Purdue University, West Lafayette, IN, 47907.
[6]Space Telescope Science Institute, Baltimore, MD, 21218.
[7]NASA Goddard Space Flight Center, Greenbelt, MD, 20771.
[8]Jet Propulsion Laboratory, California Institute of Technology, Pasadena, CA 91109.

Abstract

James Webb Space Telescope (JWST) observations of Europa's leading hemisphere reveal enhanced CO_2 abundances over equatorial chaos terrains where the subsurface ocean is thought to have breached the ice shell. Hydrogen peroxide, synthesized radiolytically by Jovian magnetospheric charged particles impinging on Europa's ice, is also elevated in these geologically active regions, spatially coinciding with CO_2. This correlation implicates CO_2 in H_2O_2 synthesis, consistent with laboratory experiments showing increased radiolytic peroxide yields in carbon-bearing ices. Our radiolysis model – which incorporates charged-particle precipitation through electromagnetic fields accounting for Europa's interaction with Jupiter's magnetosphere – predicts enhanced H_2O_2 on the leading hemisphere equatorial regions. The relative dearth of energetic electrons in this region shields peroxide from destruction, leaving a notably higher abundance towards the leading apex compared to the mid-latitude regions or the trailing side. Integrating the inferred CO_2 abundance and the associated boost in peroxide yield, we show that ocean-derived CO_2 acts as a multiplier, further elevating H_2O_2 concentrations within the fractured surfaces of Tara and Powys Regiones. Together, these results imply that geologic resurfacing at Europa's chaos terrains and precipitating radiation conspire to contribute to the excess peroxide observed by JWST, with endogenic CO_2 amplifying oxidant production in these potentially ocean-linked regions.

Confidential manuscript. © 2026. All rights reserved

*corresponding author

Introduction

Jupiter's Moon Europa is a potentially habitable ocean world. It is thought to conceal a global liquid water ocean beneath its icy crust [1–3]. Charged particles from Jupiter's magnetosphere impact Europa's icy surface [4–6], breaking water molecules to synthesize oxidants like hydrogen peroxide and molecular oxygen through radiolysis [7, 8]. Europa's ocean is estimated to be $\sim$ 100 kilometers deep lying above a rocky seafloor/mantle [9]. Geochemical cycling of water through the porous seabed can generate reductants such as molecular H_2 via serpentinization chemically reducing the ocean water [10], while also possibly enriching the ocean with carbonates or CO_2 [10, 11]. Mixing of this reduced water with radiolytic oxidants from the icy surface could generate the 'redox potential' thought to be critical to Europa's astrobiological potential. Such redox gradients could supply chemical energy that putative life forms may utilize to sustain metabolism, cellular maintenance, and reproduction [12].

The delivery of surface oxidants to the internal ocean requires surface-ocean exchange through an ice shell estimated to be 29 ($\pm$ 10) km thick [13]. Such exchange is more likely to occur at the chaos terrains where the ice shell has collapsed either from drainage of subsurface lakes [14] or been breached by the intrusive ascension of convective diapirs [15]. These geological processes emplace fresh oceanic material over the ancient surface. Generally, Europa presents a young surface ($\sim$ 40-90 Myr) with a sparse cratering record [16] suggesting that older terrains are frequently masked by fresh material resurfaced via convective emplacement [3], cryovolcanism [17], and/or tectonics [18].

The JWST observations of Europa's leading hemisphere provide compelling evidence for the presence of endogenic material and by extension, for surface-ocean exchange, at the chaos terrains. Excess carbon dioxide within Tara and Powys Regiones and relative poleward depletion suggest an internal ocean origin [19, 20]. However, it remains uncertain whether the CO_2 observed at the chaos terrains was emplaced intact from the ocean or resulted through radiolytic breakdown of oceanic carbonates and/or organics by the Jovian plasma post resurfacing events. Importantly, both scenarios trace the carbon ultimately to the internal ocean – whether as CO_2 itself or as carbonate precursors – and thus "ocean sourced CO_2" is used here in a broader sense. Though the lack of a robust detection of residual carbonate signatures [20] or its radiolysis by-products at the chaos terrains lends more support to intact resurfacing of dissolved oceanic CO_2.

Unexpectedly, hydrogen peroxide is also enhanced towards the warmer chaos terrains and decreases towards the colder mid-latitude zones [21–23]. This trend contradicts laboratory findings where colder temperatures have shown to favor the radiolytic synthesis of peroxide in pure water ice [24, 25]. We find radiolysis of Europa's leading hemisphere ice by the spatially varying magnetospheric particles, particularly energetic electrons, combined with the elevated abundance of CO_2 over the chaos terrains, control the peroxide distribution, overriding the thermal effects.

Here we present the JWST-derived maps of solid carbon dioxide and hydrogen peroxide concentrations on Europa's leading hemisphere, confirming a clear spatial link between the ocean-derived CO_2 and surface hydrogen peroxide in the equatorial chaos terrains. These equatorial regions show increased H_2O_2 relative to the mid-latitude regions – a latitudinal distribution our radiolysis model reproduces assuming a pure water ice surface [26], latitudinally varying surface temperatures [27] and spatially-varying charged particle fluxes [6, 28]. However, the tight spatial correlation between CO_2 and H_2O_2 suggests that presence of carbon could further elevate H_2O_2 concentration in the chaos regions under Jovian radiation. Laboratory experiments confirm that dilute CO_2 inclusion ($\leq$ 3%) can substantially enhance the H_2O_2 yields [29] in chaos ice analogs, by up to a factor of $\sim$ 6, compared to the 'purer' water ice at mid-to-high latitudes on Europa's leading hemisphere. Here, we constrain the H_2O_2 steady-state abundance across Europa's leading hemisphere by coupling the radiolysis model [26] with the charged-particle energy fluxes of electrons, protons, sulfur and oxygen ions in the 10 keV-100 MeV range from [6, 28]. The model assumes pure water ice and incorporates temperature-dependent H_2O_2 yields to generate a 'baseline' peroxide distribution. We then apply the laboratory-constrained, CO_2-driven enhancement factor to the 'water-ice only' baseline distribution to obtain the CO_2-boosted H_2O_2 abundance that is broadly consistent with JWST observations of leading hemisphere. These findings indicate that carbonated ocean water frozen at geologically active sites such as Tara Regio is more susceptible to magnetospheric oxidation than purer water ice. The implication for Europa's habitability is direct: an elevated oxidant supply through the fractured ices of the chaos terrains – which cover roughly one quarter of Europa's surface – would help sustain the oceanic redox disequilibria needed for biological activity.

Results

Leading Hemisphere in JWST frame

JWST observed Europa's leading hemisphere using the Near-Infrared Spectrograph (NIRSpec) [30] as part of the Cycle 1 Solar System Guaranteed Time Observations program #1250. The observations utilized NIRSpec's integral field unit (IFU) mode with a 3.0″ × 3.0″ field of view and a spatial resolution of 0.1″ per pixel. Three high-resolution gratings [G140H, G235H, and G395H] were used, covering a spectral range of 0.97-5.27 μm at a resolving power of $\sim$ 2,700; our analysis focuses on the data obtained from G235H and G395H gratings. Two dithered exposures were taken for each grating with exposures of 537 seconds each. Additional details on the GTO #1250 observation and data reduction are given in the Methods.

Figure 1 presents merged, calibrated spectra from two specific locations on Europa's leading hemisphere (LH). The black spectrum in the top panel originates from a near-equatorial pixel within Tara Regio (black pixel in Europa LH disk in the upper right inset; centroid at 17.3° S, 281.0° E) while the dark red spectrum comes from a mid-latitude location (dark red pixel; centroid at 25.3° N, 267.9° E) external to Tara Regio. The spectra are in units of radiance factor, or I/F, which is the ratio of the bidirectional reflectance of the surface to that of a perfectly diffuse surface of identical size and distance from both the Sun and the observer but illuminated at normal incidence. The incident solar flux is generated using the Planetary Spectrum Generator [31] which combines the Kurucz model [http://kurucz.harvard.edu] with Atmospheric Chemistry Experiment Fourier Transform Spectrometer (ACE-FTS) measurements over a range of 2-14 µm [32]; this composite approach has also been adopted in recent JWST/NIRSpec analyses [33].

The bottom panels of Figure 1 zoom into three key spectral windows. The sharp 2.697 µm band (bottom-left panel) is notably deeper at Tara Regio compared to the mid-latitude region, implying a locally higher CO_2 abundance at Tara Regio. The dotted lines are straight line continua across the 2.68-2.72 µm interval. Europa's 2.697 µm absorptions are well reproduced by modeled spectra [19] generated using optical constants of pure crystalline CO_2 ice [34, 35]. However, our laboratory spectra show this sharp band also persists in dilute CO_2-H_2O mixtures in both unirradiated and processed variants, with nearly identical peak position and width compared to pure crystalline CO_2 ice (Fig. S1a). It is possible that even when initially deposited as an intimate mixture, CO_2 molecules diffuse and coalesce into crystalline clusters at 70 K [36, 37]. We thus interpret Europa's 2.697 µm feature as most consistent with crystalline CO_2 clusters dispersed within bulk water ice, where the confinement within the bulk water ice helps stabilize CO_2 as a solid at Europa's surface temperatures.

The bottom-right panel of Figure 1 features the broad, double-lobed CO_2 absorption with centers near 4.25 and 4.27 µm, with both lobes clearly deeper at Tara Regio than the mid-latitude region, further reinforcing the presence of enhanced CO_2 abundance in this chaos terrain. The 4.27 µm lobe is also consistent with crystalline CO_2 ice [19, 20], supported by agreement with additional laboratory datasets [38, 39]. However, the 4.27 µm lobe also persists when CO_2 is present in dilute amounts within a water ice matrix whether as crystalline clusters or a homogenous mixture. The CO_2 inclusion induced a small ($<$ 2 nm) blueshift relative to the peak wavelength of pure crystalline film (Fig S1b). Thus, Europa's sharp 2.697 µm absorption and the 4.27 µm lobe are collectively consistent with crystalline CO_2 trapped within water ice.

The less-understood 4.25 µm lobe likely results from CO_2 in a trapped configuration, possibly within an organics-rich ice matrix or adsorbed onto salts [19, 20, 33]. Similar blueshifts in the CO_2 band position have been noted on Ganymede and Callisto [40–42], although the nature of the host materials at Europa that produce the observed shift remain unclear. The deeper CO_2 absorptions observed in Europa's leading hemisphere chaos regions have been interpreted as evidence for endogenic CO_2 source [19, 20, 43]. However, it remains uncertain whether this CO_2 was delivered intact from the ocean or produced via radiolysis of oceanic carbonates or organics by magnetospheric plasma. Notably, the 3.5 µm H_2O_2 absorption (bottom-middle panel of Figure 1) shows a similar enhancement at Tara Regio. Polynomial continua (dotted curves) were applied to the H_2O_2 bands to assess the strength of the absorption across Europa's leading hemisphere.

Spatial distribution of Solid CO_2 and H_2O_2 across Europa's Leading Hemisphere

Europa's LH disk was sampled by a subset of NIRSpec spatial pixels in the 3.0" × 3.0" field of view. Pixel footprints were projected onto Europa using the observation kernels and any pixels for which one or more of the four corners failed to intersect the surface at a valid latitude and longitude were discarded. We then

analyzed three distinct CO_2 absorptions and the 3.5 µm H_2O_2 absorption in the on-disk pixels to obtain their spatial distributions, shown in Figure 2 A-D. For each absorption, the spectrum was divided by the fitted linear continuum to compute $1-(I/F)/(I/F)_c$ and integrated over the set wavelength intervals to obtain band area. The continuum-normalized $\upsilon_1+\upsilon_3$ CO_2 band was fit with a single Lorentzian, while the υ_3 CO_2 band was deconvolved into two Lorentzian components representing the 4.25 and 4.27 µm lobes.

Retrieval of the 3.5 µm H_2O_2 band area required a higher-order polynomial to approximate the curved continuum (Figure 1). We fit a 6^{th} order polynomial over $\sim$ 3.43-3.7 µm while masking the H_2O_2 absorption region. Although this approach worked well for most pixels, several spectra corresponding to the northern pixels are distorted with multiple inflections within the absorption band (possibly due to spatial resampling of the flux and/or limb-viewing effects), making it difficult to establish a reliable continuum. These pixels were excluded from our analysis (white pixels marked by red × in Figure 2). To account for the sensitivity of the derived H_2O_2 band areas to the masking range, we systematically varied the mask about a base range and derived multiple continua for each spectrum. From these, we computed an average band area and associated uncertainties for each pixel, as detailed in the Methods. The resulting spatial distribution of the H_2O_2 band area is shown in Figure 2D. Continuum normalization yields a residual absorption with an asymmetric profile centered near 3.51 µm with a FWHM of $\sim$ 0.1 µm for most pixels, consistent with laboratory peroxide dispersed in water ice [24], and Europa's peroxide revealed by Galileo Near Infrared Mapping Spectrometer (NIMS) [7]. Though a few spectra from a small subset of pixels exhibit a slightly larger width with FWHM reaching up to $\sim$ 0.14 µm.

The distribution of CO_2 band areas overlaid on Europa's geologic map [44], reveals a notable equatorial enhancement (Figure 2). The 2.697 µm (panel A), 4.25 µm (B) and 4.27 µm (C) absorptions are prominent over Tara Regio, perhaps indicating recent geologic resurfacing. The CO_2 bands also show enhancement extending westward towards Powys Regio (most notably for the υ_3 components), perhaps associated with the Taliesin crater, which may have excavated additional carbon-bearing species to the surface. The H_2O_2 absorption shows a similar overall equatorial enhancement and notable poleward depletion (panel D), consistent with the broader pattern seen across all three CO_2 features amid pixel-to-pixel variations.

To obtain first-order estimates of CO_2 and H_2O_2 concentration, we assume these scale inversely with the effective optical path length through the ice grains, taken as the mean chord length ($2/3^{rd}$ of the diameter) of a representative 50 µm grain. This value is consistent with inferred grain sizes from spectral modeling which generally span tens to hundreds of microns, including 30-40 µm for purer leading hemisphere ice and 50-75 µm in some low albedo as well as brighter terrains [45–48]. For CO_2, band areas of the $\upsilon_1+\upsilon_3$ absorption are converted to abundance using the integrated absorption coefficient for crystalline CO_2 [49], yielding values of 0.12-0.35 % across the leading hemisphere. These values exceed previous estimates of 0.036% CO_2, derived from a representative NIMS spectrum [50], though the Galileo-era measurements had limited signal-to-noise ratio especially towards the longer wavelengths and were further degraded by the Jovian radiation [20]. For H_2O_2, the 3.5 µm band areas are similarly converted using published band strength in H_2O_2-H_2O mixtures [24, 29] resulting in an abundance of 0.1-0.4%, consistent with $\sim$ 0.13% value from Galileo NIMS data [7]. These estimates ignore grain size distributions, pixel-to-pixel variations in the JWST observation geometry, and possible spatial variations in albedo and scattering properties of ice grains across the leading hemisphere. We plot the H_2O_2 band areas against the band areas for three CO_2 absorptions in Figure S2. The linear fits confirm a positive correlation [22], supporting the idea that endogenic CO_2 may influence radiolytic peroxide synthesis in the icy grains of Tara and Powys Regiones.

Discussion

Excess radiolytic H_2O_2 in CO_2-infused ice: Insights from the Lab

Motivated by the strong correlation between Europa's CO_2 and H_2O_2 observed by JWST, we conducted laboratory irradiation experiments on water ice films infused with trace amounts of CO_2 [29] (instrumentation and methodology detailed therein). In brief, water ice films with varying CO_2 concentrations ($<$ 10 %) were deposited at 70 K and irradiated with 10 keV electrons at 70 and 100 K. The steady-state H_2O_2 concentration in CO_2-bearing ice films was substantially higher, up to 6×, than in pure water ice. The H_2O_2 enhancement increased steadily with CO_2 concentration plateauing above $\sim$ 3% at both temperatures (Figure 3A). The inflating effect of CO_2 was stronger at 100 K, the approximate temperature of Europa's

equatorial chaos regions [27]. The enhancement is possibly due to the electron scavenging nature of the CO_2 molecules [51] which are thought to capture radiolytically-generated secondary electrons that would otherwise contribute to the peroxide destruction. The quenching of H_2O_2 destruction in CO_2-infused ice is reflected in the sharp reduction in the peroxide destruction cross section with CO_2 concentration [29].

Using the CO_2 abundance inferred from the $\upsilon_1+\upsilon_3$ band (Figure 2A), together with the latitude-dependent diurnal-average surface temperatures [27], we map the expected CO_2-driven peroxide enhancement factor across Europa's leading hemisphere at JWST spatial resolution (right panel of Figure 3). Within the equatorial chaos regions, the enhancement factor peaks near ~ 1.6 in regions with abundant CO_2, indicating a substantial CO_2-driven boost in peroxide abundance. The enhancement factor approaches 2, if smaller grains ($\sim$ 30 µm) are assumed at the chaos terrains. By contrast, the enhancement factor drops to $\sim$ 15% toward 60° N/S, showing the effect to be weaker at the cooler, CO_2-poor mid-latitude zones. We note that Europa's surface is irradiated by charged particles other than 10 keV electrons used in our experiments [29]. The CO_2-driven enhancement in H_2O_2 yield is primarily a function of the CO_2 abundance and its ability to reduce H_2O_2 loss by scavenging off secondary 'delta' electrons. Potential variations in the enhancement factor with projectile species and their energies are yet to be constrained experimentally, and here we adopt the 10 keV value.

Europa's baseline H_2O_2 distribution

Forward modeling of Europa's surface peroxide distribution has now become feasible, owing to advances in both understanding water-ice radiolysis from laboratory experiments and charged-particle precipitation modeling of the Europan magnetospheric environment [6, 52, 53]. Specifically, previous works [6, 28] trace electron, proton, O^{2+}, and S^{3+} ion trajectories (10 keV - 100 MeV) through realistic electromagnetic fields generated by a multifluid magnetohydrodynamic model [54] that treats Europa as electromagnetically active rather than inert [55], incorporating field-line draping by the corotating plasma's interaction with the moon's O_2 atmosphere, as well as the induced magnetic field from currents in the subsurface ocean. On the radiolysis side, analysis of decades of experiments [26] revealed how peroxide production and destruction depend on irradiation projectile parameters and ice temperature. The analysis indicated the H_2O_2 creation yield G_p (H_2O_2 molecules produced per eV) and destruction cross section σ_d to be fairly constant across projectile species and energies, with an exponential decline in the creation-to-destruction ratio (which controls the peroxide abundance at steady state) at higher temperatures. This framework has been applied to estimate radiolytic peroxide concentrations and transport through the Enceladus crust to its subsurface ocean, owing to burial under plume fallout [56]. We adapt it here (minus the burial) to estimate peroxide distributions across Europa's surface.

Using particle fluxes vs. energy from [6, 28] as input, we compute the combined energy deposition rate (eV H_2O molecule^{-1} yr^{-1}) from magnetospheric particles (electrons and ions, 10 keV-100 MeV) as a function of depth into Europa's ice versus surface location, based on the average stopping power S of each particle as they slow down and stop within the ice [57]. This absorbed power breaks apart water molecules to make OH radicals which combine to form peroxide. Though not all dissociated OH radicals contribute to H_2O_2 synthesis as a large fraction recombine with H to reconstitute H_2O, particularly in the solid state where the surrounding matrix confines the dissociated fragments promoting geminate recombination. Competing with synthesis is simultaneous peroxide destruction by all projectiles, which scales with the total particle number flux F, through a near-constant destruction cross section σ_d of $10^{-14.1\ (\pm 0.6)}$ cm^2 [26]. The error in the exponent captures the spread in the cross section reported in different studies [26 and references therein]. The steady-state peroxide concentration as a function of depth then follows from the ratio of total creation to total destruction rates, incorporating Europa's diurnally averaged surface temperature distribution [27]. Averaging the peroxide concentration over the top ~50 µm – the approximate optical sensing depth – as a function of latitude and longitude yields a global H_2O_2 concentration map produced by radiolysis of pure water ice (i.e. excluding the effects of CO_2). In a prediction consistent with the trend observed by JWST, the modeled peroxide concentration peaks towards the equator on the leading side (Figure 4).

To understand this result, it is important to recognize that H_2O_2 is more fragile than H_2O against radiation. Nearly pure solid hydrogen peroxide under 50 keV H^+ irradiation rapidly decomposes with a large destruction yield $\sim 21(\pm 5) \times 10^{-3}$ H_2O_2 per absorbed eV [58], far exceeding the creation yield G_p of $\sim 10^{-3}$ H_2O_2 per eV absorbed in water ice [26]. For dilute peroxide in ice, compiled experimental data shows

a destruction cross section that is largely independent of projectile species and energies, and remains ~ 1-2 orders above the creation cross section, yielding low equilibrium peroxide concentrations typically < 1% relative to water ice. The largely energy-independent nature of the destruction cross section implies that projectiles readily destroy peroxide molecules in their track with high efficiency regardless of their energies, and that the peroxide destruction rate scales with particle number flux traversing the ice. By contrast, peroxide creation is a far less efficient, energy-limited process, that scales with the total absorbed energy [26]. This distinction between flux-driven destruction and energy-driven creation is key to understanding Europa's peroxide distribution.

Europa's surface is impacted nearly uniformly by high-stopping power projectiles (> 1 MeV heavy ions) that deliver large energy doses into relatively fewer water molecules within a shallow surficial layer, driving peroxide synthesis to a similar steady-state value across the global surface [6, 28]. However, regions, like the trailing side, bombarded with a larger number of low-stopping power particles (i.e. 10-100s of keV electrons) suffer disproportionate destruction relative to creation, suppressing the equilibrium peroxide concentration (Figure S3). These energetic electrons are more penetrating: many more electrons than ions pass beyond the ~50 µm optical sensing depth, so their net effect over this layer is to overwhelmingly destroy peroxide rather than synthesize it. The leading apex, located in Europa's plasma wake, receives a reduced flux of these destructive electrons, allowing the energy deposited by the heavy ions to build higher peroxide concentrations there.

These competing effects are captured in Figure 4. The absorbed power that drives the peroxide synthesis is slightly depleted at the leading apex: ~ 1.25× lower than at the leading mid-latitudes and ~ 1.4× lower than at the trailing apex (Figure 4A). However, the total particle number flux F within the sensing depth shows an even steeper leading-apex deficit, falling ~ 3.5× below the mid-latitudes and nearly 8× below the trailing apex. Averaged over the top 50 µm and accounting for the falloff in flux as particles decelerate and stop, the total flux F in the optical skin is dominated (~ 90%) by ~10 keV – 1 MeV electrons. Because these electrons preferentially strike the trailing hemisphere [5, 28, 59], the H_2O_2 destruction rate constant ($F \times \sigma_d$) is ~ 8× higher at the trailing apex than at the leading apex (Figure 4B). Destruction rates of 1 – 27 yr^{-1} across Europa's surface imply a peroxide survival lifetime of months at most – ~ 8 months towards the leading equator, ~ 2 weeks on the trailing side. The H_2O_2 molecules detected by JWST aren't a relic; they form a standing population, destroyed and resynthesized several times over in a single year.

Within the leading hemisphere – the region covered by the GTO #1250 observations – the interplay between absorbed power and the destruction rate produces a clear equatorial maximum in the steady-state H_2O_2. Although both quantities decrease from mid-latitude towards apex, the flux drops more steeply (~ 3.5×) than the power (~ 1.25×). Consequently, the ratio (absorbed power/destruction rate) is highest in the equatorial band of the leading hemisphere (Figure 4C). The reduction in destructive electron flux, which is inefficient at driving radiolysis, tips the creation-destruction balance in favor of net peroxide accumulation towards the leading apex. This explains the elevated H_2O_2 abundances over the equatorial chaos over mid-latitude regions, consistent with JWST observations.

At steady state, the H_2O_2 production rate – G_p × absorbed power – is balanced by the destruction rate, $\sigma_d \times F \times$ (H_2O_2 fractional abundance). The absorbed power is the product of F and the stopping S. The equilibrium H_2O_2 abundance thus reduces to $S \times G_p/\sigma_d$. Decades of water-ice radiolysis experiments compiled in [26], provide fluence dependence data of H_2O_2 synthesis, from which the G_p/σ_d ratio can be deduced across Europa-relevant temperatures. This ratio shows an exponential decline with temperature T, which we fit as $(G/\sigma_d)_o\ e^{-\alpha T}$, with the electron irradiation data [29] added to the compilation (Figure S5). The fit yields $\alpha = 0.013\ (\pm\ 0.0041)\ K^{-1}$ and $(G/\sigma_d)_o = 3.55 \times 10^{11}\ eV^{-1}\ cm^{-2}$ with the compiled measurements scattering about this relation over a 1σ interval of $1.6 - 7.7 \times 10^{11}\ eV^{-1}\ cm^{-2}$. Multiplying by the flux-weighted stopping S, in units of eV cm^2, averaged over the top 50 µm sensing depth, we obtain the temperature-dependent 'baseline water-ice only' H_2O_2 concentration, $(G/\sigma_d)_o\ S\ e^{-\alpha T}$. Figure 4D shows Europa's baseline global steady-state peroxide concentration evaluated at the upper bound of the scatter interval, with α held at 0.013 K^{-1}.

Extending these analyses globally, our model predicts that the trailing apex - despite receiving ~ 1.4× more absorbed power and nearly ~8× higher particle flux than the leading apex - should exhibit an equilibrium H_2O_2 concentration an order of magnitude below the global maximum, which occurs near the leading equatorial region (Figure 4D). The destruction rate far outpaces creation such that the peroxide abundance

towards the apex and more generally over the trailing hemisphere is suppressed (Figure 4D), consistent with reported hemispherical difference in H_2O_2 abundance [60]. This result is counter to the conventional expectation that more intense bombardment of the corotating plasma over the trailing hemisphere should translate to higher peroxide concentration. Instead, the steady-state H_2O_2 abundance is modulated by the balance between creation and destruction rather than irradiation flux alone.

Two important caveats merit emphasis. First, the suppression over the trailing hemisphere is due to the fragile nature of H_2O_2 molecule (O-O bond strength $\sim$ 2 eV, half the O-H strength in H_2O) which makes it prone to radiolytic destruction. More robust species (e.g. H_2SO_4 and its hydrated forms) may resist destruction more effectively and therefore may display a different spatial distribution, one not necessarily suppressed in regions of elevated electron flux. Second, the trailing hemisphere is markedly depleted in water ice, with non-ice components such as salt and acid hydrates reaching abundances as high as 65-85% [61, 62]. The scarcity of water ice will likely result in an even lower equilibrium peroxide concentration compared to our model prediction which does not account for the provenance of acid hydrates. However, the bound water molecules may still participate in radiolysis and contribute to the peroxide abundance.

Although the leading-hemisphere equatorial chaos ices are the warmest on Europa – which suppresses peroxide synthesis [24, 26] – the latitudinal (equatorial vs. polar) asymmetry in the impinging radiation, particularly in the electron flux, is the primary modulator of the 'baseline water-ice only' peroxide distribution. Including Europa's diurnally averaged surface temperatures [27] in our model, the thermal suppression is insufficient to displace the peroxide maximum from the leading apex (Figure S4). The model predicts a peak concentration of 0.15% H_2O_2 near the leading apex. Degraded to JWST pixel scale, this falls to 0.11%, which is $\sim 2.4\times$ below the 0.27% at the collocated pixel (Figure 2D). We discuss next how the inclusion of endogenic CO_2 in the radiolyzed optical skin may help bridge this deficit.

Endogenic CO_2 as a Peroxide Booster over Europa's leading chaos terrains

Applying the H_2O_2 enhancement factor (Figure 3B) to the baseline peroxide map increases the modeled steady-state H_2O_2 abundance by ~60% over the equatorial leading hemisphere chaos terrains. This increase could plausibly be higher, if smaller ice grains ($\sim$ 30 µm vs. nominal 50 µm assumed here) are more prevalent or if CO_2 is more concentrated at smaller local scales. Furthermore, the current CO_2 estimate does not include carbon associated with the 4.25 µm absorption. If CO_2 trapped in an organic matrix or adsorbed on salts or other host materials were to roughly double the carbon inventory over the chaos terrains, the H_2O_2 boost factor could exceed 3, bringing the modeled H_2O_2 abundance closer to JWST-inferred levels, while noting that both enhancement factor and abundance assessments remain approximate, first-order estimates. We present the CO_2-boosted peroxide map degraded to the coarser JWST resolution in Figure 4E. The peroxide abundance peaks at ~0.19% at 285° E on the equator, within ~40% of the 0.27% JWST value at the collocated pixel - agreement at the level the dispersion in G_p/σ_d dataset allows.

Both the observed and modeled H_2O_2 abundances decline poleward, by factors of $\sim$ 1.4 and ~1.8 respectively between equator and 40° N/S. In longitude though, the model diverges from the observation. The modeled abundance falls off by $\sim 2\times$ westward of the leading apex (from 0.11% near 270°E to ~0.05% towards 220°E), whereas the observations rise over the same span increasing towards Powys Regio from 0.22% to 0.27%. The highest observed abundance ~ 0.4% is at 217°E and 16°S, close to Taliesin crater at 223°E and 23°S. This longitudinal excess towards the western limb may reflect a true compositional contribution from Taliesin's ejecta or limb sampling effects or both.

Several other factors that are not included in our model could also influence Europa's H_2O_2 abundance. For example, NaCl appears to be enhanced over the chaos terrains [63], but its role in modulating H_2O_2 concentration is not known and requires irradiation experiments with CO_2 embedded in briny ices. Taking these caveats into consideration, the CO_2-enhanced model result nonetheless captures the broad peroxide distribution across Europa's leading hemisphere and predicts the trailing peroxide abundance in the vicinity of the apex to be $\sim 6\times$ smaller than the leading counterpart, while not accounting for potential suppression from enrichment of salt and acid hydrates/H_2O ice depletion on the trailing side, or the boosting effect of any trailing hemisphere CO_2. The endogenic CO_2-derived boost factor enables the model to approach the observed leading hemisphere peroxide level, underscoring CO_2's role as a key modulator of Europa's surface oxidant budget.

Conclusion and Outlook

This work provides important insights into the mechanisms by which geologic activity at chaos terrains and charged particles in the Jovian magnetosphere work synergistically to enhance the synthesis of radiolytic oxidants such as hydrogen peroxide in Europa's icy crust. Geologic processes emplace carbon-bearing water from the interior ocean to the breached surfaces of the chaos terrains, where it is subject to energetic charged particles from Jupiter's magnetosphere. The resulting surficial CO_2 enhances the radiolytic yield of H_2O_2, and presumably other oxidants, as demonstrated through the laboratory experiments, leading to the observed co-enhancement of CO_2 and H_2O_2 at Tara and Powys Regiones by JWST. The peroxide distribution across Europa's leading hemisphere surface is determined not just by the surface temperature but more importantly by the emplacement of fresh oceanic carbon-bearing material and spatially asymmetric (across latitude and longitude) impingement of Jovian magnetospheric particles, particularly the 10-100s keV electrons. Our findings highlight the complex interplay between the interior ocean, geologic activity and radiation in shaping Europa's surface chemistry and composition, driving redox gradients critical for its potential habitability.

The impact of brines such as NaCl on ice radiolysis remains unclear and further experiments are needed to investigate their effects on oxidant yields in Europa's icy crust. Recent models indicate that brine percolation channels can expedite the transport of oxidants through the icy crust, potentially delivering $\sim 85\%$ of radiolytic oxidants to the subsurface ocean over timescales of ˜ 20,000 years [64]. This rapid brine-assisted oxidants delivery could be important for sustaining oceanic redox gradients which is key to Europa's potential habitability. Recent models, however, indicate a silent seafloor with limited volcanism and water-rock interactions, potentially choking the mantle-derived reductant supply into the ocean [65, 66]. The diminished reductant yield can adversely affect the ocean's habitability, especially if only oxidants are delivered to the ocean from the ice shell. However, the radiolysis of CO_2-containing chaos ice could also lead to production of CHO-bearing species like methanol or carbonic acid as laboratory studies indicate [29]. A subset of leading-hemisphere pixels show subtle evidence of excess absorption on the long-wave shoulder of the peroxide band, but this excess shows no systematic spatial trend and its position does not agree with methanol or carbonic acid [29, 33, 67, 68], precluding a confident assignment. It is possible, however, that the presence of salts may shift band positions and distort the spectral profile of CHO-bearing species. Radiolytic synthesis of organics alongside peroxide would make the ice shell a source of both oxidant and reduced organics to the ocean, potentially bypassing the need for seafloor reductants. Whether such a supply could sustain biological activity would still depend on yields, redox energy and delivery rates to the underlying ocean. Upcoming missions like Clipper and Juice are equipped to constrain these hypotheses further.

The relevance of our investigation, which leverages laboratory findings to elucidate the role of endogenic CO_2 in controlling peroxide distribution observed by JWST, extends to future missions, particularly to Europa Clipper. Equipped with a comprehensive remote sensing package, Clipper will utilize the Mapping Imaging Spectrometer for Europa (MISE), Europa Imaging System (EIS) and Europa Ultraviolet Spectrograph (Europa-UVS) to collaboratively analyze Europa's surface composition at unprecedented spatial and spectral resolution, mapping the distribution of ices, acid and salt hydrates, and organics. Likewise, MASPEX and SUDA will measure and map the composition of more complex species (including organics, salt and acid hydrates) at larger scales through in-situ collection of gases and icy grains. Clipper will validate and build upon these JWST findings to improve our knowledge of surface-ocean exchange and oxidant production at Europa's enigmatic chaos regions.

Figures

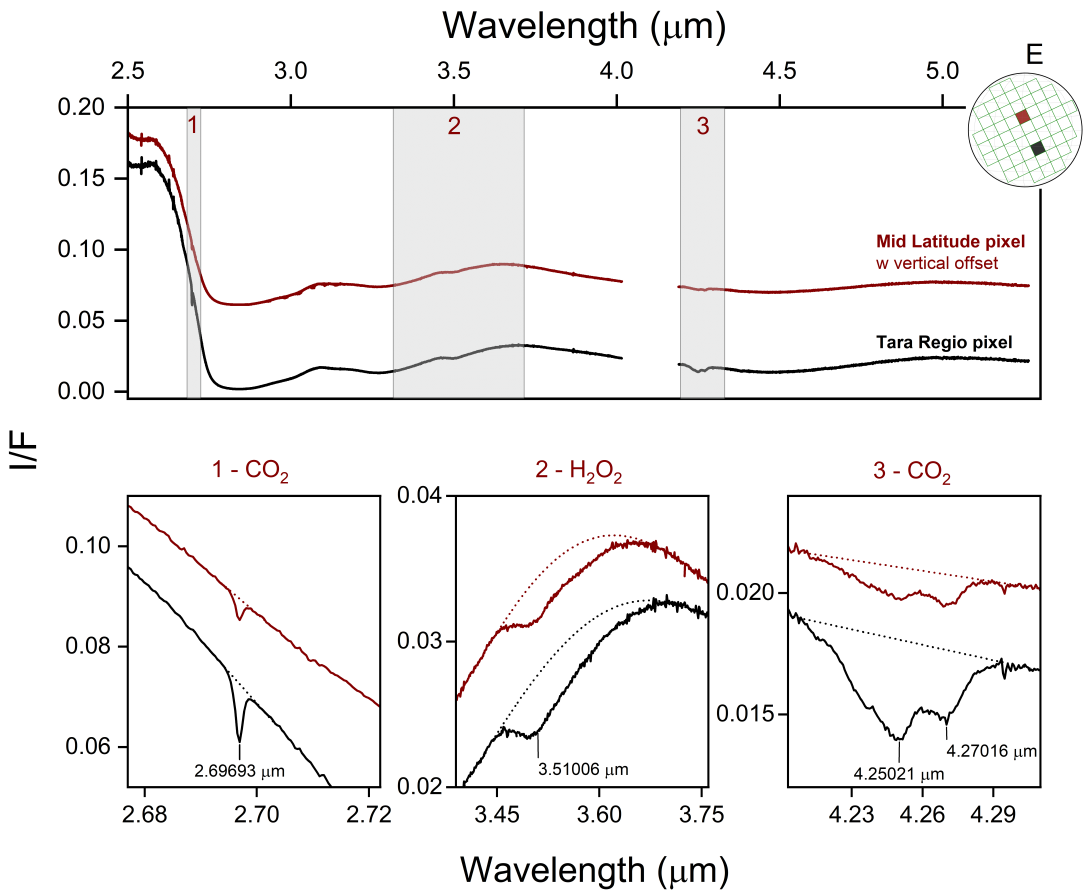


Fig. 1 Spectral signatures of excess CO_2 and H_2O_2 at Tara Regio. JWST reflectance spectrum from a Tara Regio pixel [black spectrum, pixel indicated by the black square in the Europa inset (E) at the top right corner] compared to a spectrum from a mid-latitude pixel [dark red curve]. The occurrence of CO_2 is evident from the sharp absorption at 2.697 μm ($\upsilon_1 + \upsilon_3$ mode) shown in the bottom left panel. The 4.27 μm absorption in the bottom right panel is due to solid CO_2 (υ_3 fundamental mode). Both the 2.7 and 4.27 μm absorptions are consistent with CO_2 in either pure state or when intimately mixed in with water ice. The 4.25 μm absorption (also bottom right) has been tentatively ascribed to a 'complexed form' of CO_2, either adsorbed on brines or embedded in organics-rich ice matrix [19]. All three CO_2 bands present deeper absorption in the Tara Regio spectrum than the mid-latitude spectrum. Interestingly, the asymmetric 3.51 μm H_2O_2 absorption is also stronger in Tara Regio spectrum (bottom middle panel). Our experiments implicate endogenic CO_2 to inflate radiolytic synthesis of peroxide contributing to the observed peroxide excess in Tara Regio compared to the mid latitude regions with purer water ice content.

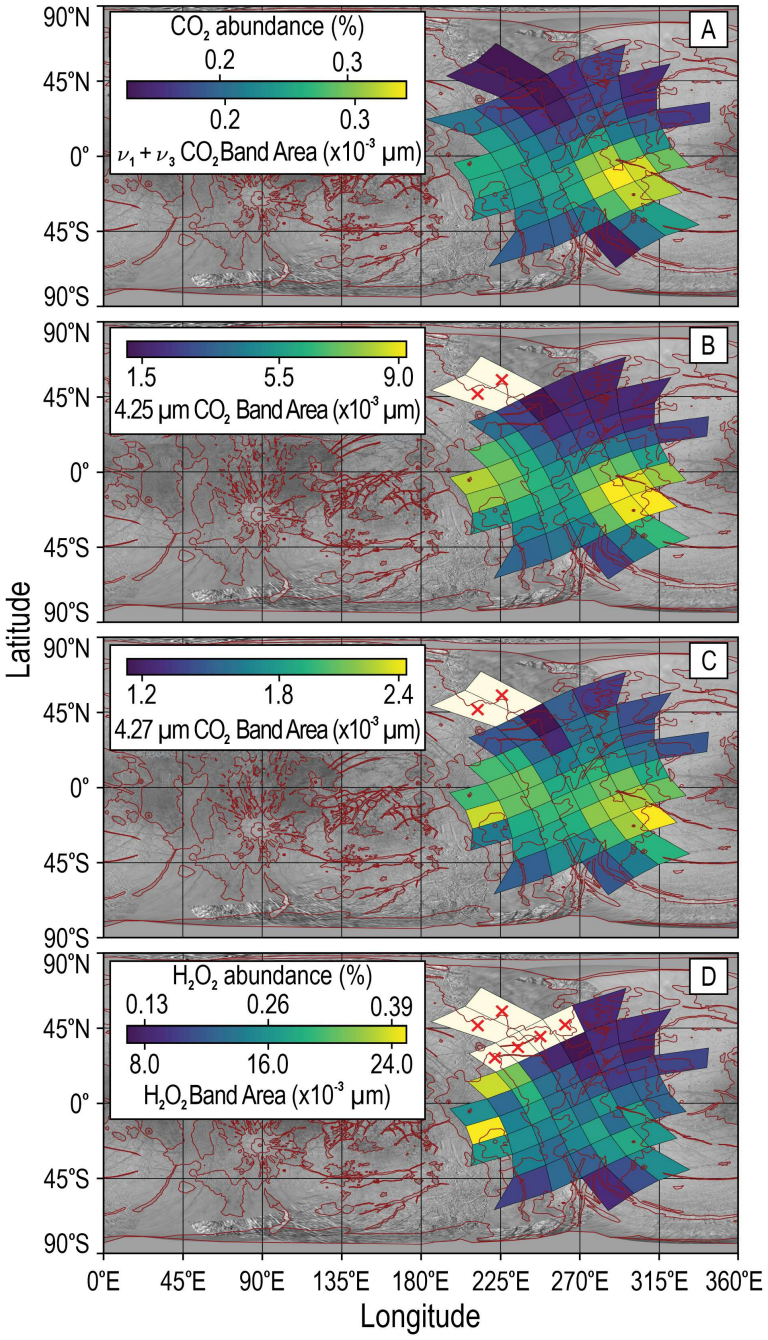


Fig. 2 Overlays of CO_2 and H_2O_2 absorptions atop Europa's Geologic Map. Panels A-C show the spatial distribution of integrated band areas for three CO_2 absorptions, highlighting equatorial enhancement at Tara and Powys Regiones. Mid-latitude regions ($> 30°$ N/S) appear relatively depleted in CO_2 compared to the equatorial chaos terrains. Panel D shows the distribution of the 3.5 µm H_2O_2 absorption, which closely mirrors the three CO_2 maps.

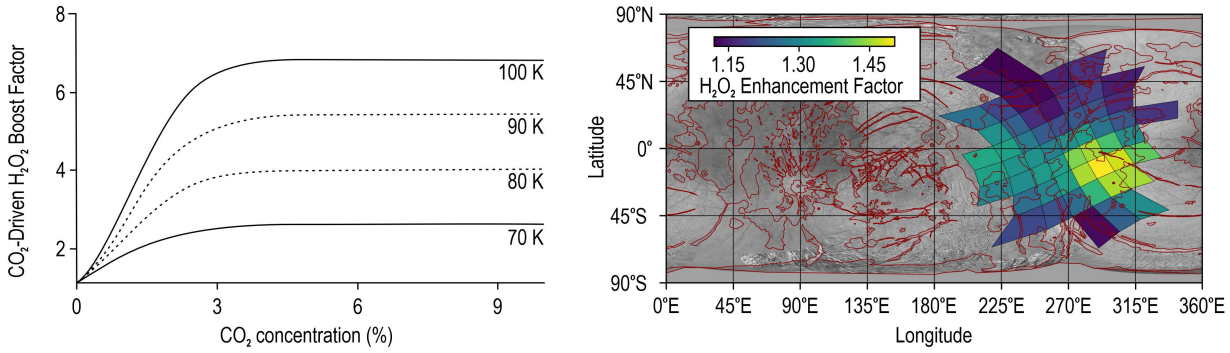


Fig. 3 CO_2-boosted radiolytic H_2O_2 enhancement factor in icy Chaos analogs. Left panel shows the experimentally derived H_2O_2 enhancement curves as a function of CO_2 concentration in water ice films irradiated with 10 keV electrons at 70 and 100 K [29]. Dotted curves are linearly interpolated enhancement factors for intermediate Europa surface temperatures. Right panel shows the map of CO_2-enabled H_2O_2 enhancement factor at JWST spatial resolution, computed using the average CO_2 abundance and the mean diurnal surface temperature in each pixel.

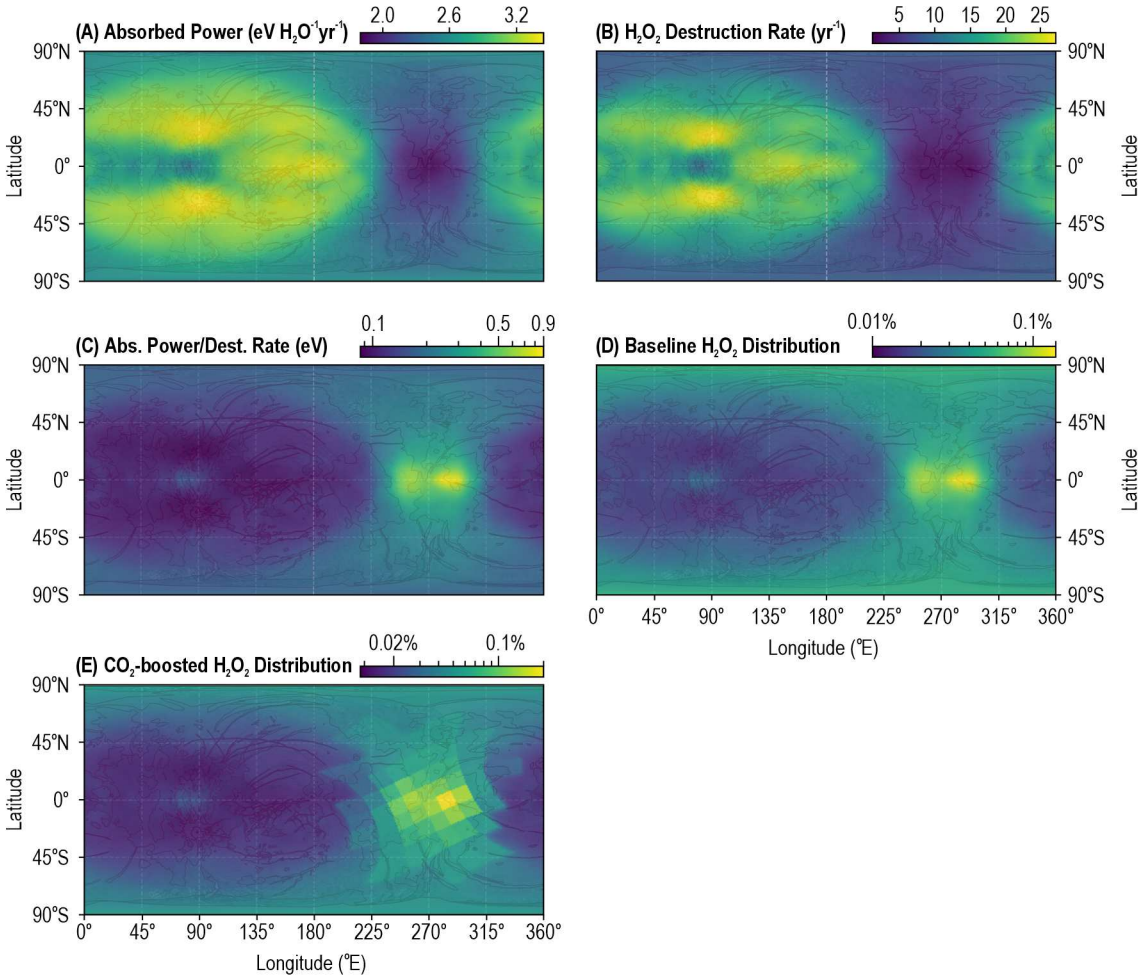


Fig. 4 Europa's Peroxide. H_2O_2 creation is driven by the absorbed power per H_2O molecule (mapped in panel A) from electrons and all ion species of all energies (10 keV-100 MeV) averaged over the 50 µm optical skin. Likewise, the destruction rate per H_2O_2 molecule (panel B) is proportional to the depth-averaged total particle flux F of all particles traversing the ice, multiplied by the constant destruction cross section σ_d, adopted to be $10^{-14.1}$ cm^2. The predicted equilibrium peroxide concentration (panel D, excluding the effects of CO_2) is proportional to the depth-averaged ratio (panel C) of absorbed power to destruction rate. Peroxide concentrations peak at the leading hemisphere equatorial region, where the reduced energetic (>10s of keV) electron flux results in a low destruction rate (large ratio in C). Carbon dioxide contributes to additional peroxide on the leading side (panel E), mostly consistent with JWST observations (Figure 2D). The modeled maps are smoothed with a 5° Gaussian kernel, which slightly lower the peak values relative to native 1° grid.

Methods

JWST GTO 1250 Observations and Data Reduction

Europa was observed with the Integral Field Unit (IFU) of the Near-Infrared Spectrograph (NIRSpec) onboard the James Webb Space Telescope (JWST) as part of the Cycle 1 Guaranteed Time Observations (GTO) program #1250. The IFU mode provides a 3.0 arcsec × 3.0 arcsec field of view sampled at 0.1 arcsec per pixel. Observations employed the high-resolution gratings G235H and G395H, paired with the F170LP and F290LP filters, respectively, covering wavelength ranges of 1.66–3.17 µm and 2.87–5.27 µm at a resolving power of approximately 2700 [30]. Two dither positions were acquired for each grating configuration, improving the subsampling to 0.05 arcsec per pixel. These configurations capture diagnostic absorption bands of H_2O, CO_2, and organics across Europa's leading hemisphere.

Our reduction of the JWST data closely followed the methodology described by [33, 69]. The uncalibrated data were retrieved from the Mikulski Archive for Space Telescopes and processed locally using Stages 1 and 2 of the JWST calibration pipeline (version 1.17.0) [70], producing flat-fielded, distortion-corrected, wavelength- and flux-calibrated data cubes expressed in units of MJy sr^{-1}. Reference files were automatically drawn from the Calibration Reference Data System (CRDS) context jwst_1321.pmap. The processing included correction of correlated detector noise using the NSClean algorithm implemented in the standard pipeline [71]. Stage 3 of the JWST calibration pipeline was then applied to generate a dither-combined cube per grating.

The centroid of Europa within the NIRSpec field of view was determined from a two-dimensional image obtained by collapsing the entire spectral cube along the wavelength axis, after masking pixels with non-zero data-quality flags. The centroid position was measured by fitting a two-dimensional Gaussian model to the target point-spread function (PSF). To identify and mask outliers in the background region, we masked a 17 × 17 pixel spectral extraction region centered on the target in each wavelength slice and applied two-dimensional iterative sigma clipping, which removed pixels deviating by more than 8σ from the median in either direction. This procedure removed background outliers while preserving Europa's PSF, and no additional filtering was applied along the wavelength axis.

After masking outliers, background subtraction was carried out on a slice-by-slice basis. For each wavelength, the mean background level was determined from pixels outside a 25 × 25 pixel region centered on the target, after applying five iterations of 8σ clipping. The resulting mean background was subtracted from each image slice, and the associated uncertainty, estimated as the standard error of the mean, was propagated in quadrature into the pixel flux uncertainties.

The background-subtracted NIRSpec cubes, expressed in spectral radiance units (MJy sr^{-1}), were converted to dimensionless reflectance ($\frac{I}{F}$) at the pixel level. The conversion follows $\frac{I}{F} = (\pi r_h^2 I)/F_\odot$, where I is the observed spectral radiance of each pixel, $F_\odot$ is the solar flux at 1 AU, and r_h is the heliocentric distance of Europa at the time of the observation (4.95 AU). The solar spectrum used for this calculation is the one implemented by the Planetary Spectrum Generator (PSG) [31], which combines the Kurucz solar model at wavelengths shorter than 2.0 µm (http://kurucz.harvard.edu) with measurements from the Atmospheric Chemistry Experiment Fourier Transform Spectrometer (ACE-FTS) onboard SCISAT-1 over the 2–14 µm range [31, 33]. Prior to division, the solar spectrum was convolved to match the wavelength-dependent resolving power of the NIRSpec dispersers. Each pixel I/F spectrum was passed through a 21-point-wide 5σ rolling median filter along the wavelength axis to mask isolated outliers.

The pixel I/F spectra and associated uncertainties obtained from the G235H/F170LP and G395H/F290LP cubes were concatenated, preserving each grating's native sampling. Before merging, we applied a quality filter based on the distribution of relative uncertainties: for each spectrum we computed the relative error across flux-positive samples, estimated the mean and standard deviation using sigma-clipped statistics (3.5σ), and removed points with relative error exceeding the high-tail threshold of mean + 8σ.

Selection of Europa's on-disk pixels

SPICE kernels [72] were used to constrain observation geometry for JWST observations of Europa, including SPK (ephemeris), PCK (planetary constants), CK (spacecraft orientation), FK (reference frames), and IK (instrument FOV), to determine the spatial relationship between the observer and the target. To calculate per-pixel geometry, a vector for each individual pixel within the 3" x 3" field of view was projected onto

Europa's surface using the *sincpt* (surface intercept) function. This allows for the determination of the incidence, emission, and phase angles at every point on the disk by calling routines like *ilumin* and others, which account for the target's triaxial ellipsoid shape and rotation. The pixel intercepts are constrained by projecting the four corners of the FOV polygon (found with *getfov*) onto the planetary surface to define the exact footprint and ensure the observation's spatial extent is accurately mapped to Europa longitude and latitude.

υ_1+υ_3 CO_2 band area retrieval

To obtain the 2.697 µm CO_2 band area map, we fit a local continuum around the absorption feature using two fixed wavelength windows bracketing the band (2.690-2.694 µm and 2.699-2.703 µm). Iterative 2.5σ-clipping (MAD-based, ≤ 3 iterations) is applied within each window to remove outliers; the surviving points from both windows are combined and fit with a single straight line. Examples of such continua are shown in Figure 1 in the main section. Each spectrum is then divided by this continuum to produce the normalized absorption spectra, which is given by $1 - [(\mathrm{I/F})/(\mathrm{I/F})_c]$. Since the continuum is treated as fixed, the pointwise uncertainty on the absorption depth is $(\mathrm{I/F})_{err}/(\mathrm{I/F})_c$, where $(\mathrm{I/F})_{err}$ is the error in the I/F spectra.

Before fitting, isolated single-point spikes within the absorption band are detected and masked using a first-derivative impulse test: a point is flagged if both adjacent finite differences are large ($> 8\sigma$ of the MAD scatter of all first differences) and of opposite sign, indicating a sharp spike-and-return pattern. Flagged points are set to NaN so the fitter ignores them. The normalized, spike-cleaned absorption is modelled with a Lorentzian profile with a fixed-center fit (center locked to a pre-determined median value of 2.6968 µm from a prior all-pixel run). Both fits are performed iteratively with 5σ residual clipping (up to 3 iterations) using scipy.optimize.curve_fit with bounded parameters.

For each pixel, the CO_2 band area is computed in two ways over the fit range: trapezoidal integration of the spike-cleaned data, and trapezoidal integration of each best-fit Lorentzian model. Monte Carlo uncertainties on the model-integrated areas are estimated by perturbing I/F with Gaussian noise drawn from the measurement errors (300 draws), refitting the full continuum + Lorentzian pipeline each time (with the same spike mask held fixed), and taking the 16^{th}-84^{th} percentile half-width of the resulting area distributions. We present the best-fit band area obtained from trapezoidal integration of the Lorentzian fit in Figure 2A. Goodness-of-fit metrics (RMSE, χ^2, reduced χ^2, DOF) are computed for the continuum and the Lorentzian fit approach.

υ_3 CO_2 4.25-4.27 µm band area retrieval

To obtain the band areas for the absorption components centered near 4.25 and 4.27 µm features that constitute the broad double lobed υ_3 band, we first fit a linear continuum over two windows flanking the doublet (4.189-4.206 µm and 4.31-4.34 µm). Within the continuum windows, isolated single-point spikes are first removed via a first-derivative impulse test, and the surviving points are then iteratively σ-clipped (2.5σ, up to 3 iterations) prior to fitting a straight line. An example of such continuum is shown in Figure 1 in the main section. Since the continuum is treated as fixed, the pointwise uncertainty on the absorption depth is $(\mathrm{I/F_{err}})/(\mathrm{I/F})_c$. A second pass of derivative-based spike masking is applied to the normalized profile within the band region (4.206–4.31 µm) before fitting.

We deconvolved the double-lobed CO_2 absorption using a sum of two Lorentzian peaks, with the component centers locked at pre-determined median values of 4.2462 and 4.2711 µm (25 nm separation) and the FWHM of the 4.27 µm component fixed at 16 nm, consistent with our laboratory measurements (Fig. S1). Locking the centers prevents the optimizer from trading amplitude for position in the blended doublet, and fixing the 4.27 µm component width further constrains the decomposition. Among the model variants tested (see below), this configuration yielded the best goodness-of-fit metrics. Each fit is performed iteratively with 5σ residual clipping (up to 3 iterations) using bounded least-squares via scipy.optimize.curve_fit. For each pixel, the CO_2 band area is computed by applying trapezoidal integration of each component over the band region, the trapezoidal integration of each model component and the analytic integration of each model component. We present the trapezoidal integration of the model components in Figure 2 of the main text.

Monte Carlo uncertainties were estimated by perturbing the I/F spectra with Gaussian noise drawn from the reported errors (300 draws), re-running the full continuum + spike mask + deconvolution fit pipeline

each draw, and reporting half width of the resulting area. Goodness-of-fit metrics (RMSE, χ^2, reduced χ^2, DOF) are computed for the continuum and the double Lorentzian fit approach. We note that we also investigated deconvolution alternatives, including double Gaussian, mixed Gaussian-Lorentzian models, as well as variants with fixed and free centers and free FWHM of the long-wavelength component. We find that the 4.27 µm component is more sensitive to the choice of model flavor than the 4.25 µm component.

3.5 µm H_2O_2 band area retrieval

For the 3.5 µm H_2O_2 band-area map, the analysis differs from the CO_2 bands, in that no parametric absorption model is assumed; the band area is instead measured empirically from the continuum-divided spectrum. At each pixel, we isolate the spectral region spanning 3.35-3.90 µm and model the local continuum with a 6^{th} degree polynomial fit to the data outside the band window (3.43–3.69 µm). Spikes are first detected via a rolling-median filter (11-point window, 8σ threshold) and excluded from the fit. The polynomial is then fit iteratively with 2.5σ clipping ($\leq$ 15 iterations) to suppress residual outliers in the continuum regions. Each spectrum is divided by this continuum to produce the continuum-divided profile $(I/F)/(I/F)_c$. As a quality gate, any continuum solution for which the 99th percentile of $(I/F)/(I/F)_c$ exceeds 1.04 across the fit domain is rejected, ensuring the polynomial does not dip below the data and produce spurious emission-like artifacts.

From the continuum-divided spectra within the absorption window, we extract the band depth, band center, FWHM (from half depth crossing from the smooth profile) and band area, computed as the trapezoidal integration of the unsmoothed data. To quantify the sensitivity of the band areas to the choice of the masking window flanking the absorption region, we employ a mask-window ensemble. A grid of candidate masking windows is generated by perturbing the nominal mask window edges by ±0.02 µm in steps of 0.005 µm, and a random subset of 60 windows are drawn from this complete 81 masking window set. For each candidate window, the full polynomial continuum fit is repeated and the resulting divided spectrum is subject to a series of acceptance criteria: a minimum number of fit points before and after clipping, a maximum clipped fraction, the percentile gate on $(I/F)/(I/F)_c$ described above, and a requirement that the continuum-divided spectrum agree with unity to within 1% (RMS) outside the band. Band metrics, including areas, are computed for each accepted realization, and the ensemble spread (standard deviation and 16^{th}-84^{th} percentile range) captures the systematic uncertainty due to the choice of the continuum.

Monte Carlo uncertainties due to measurement noise are estimated separately by perturbing I/F with Gaussian noise drawn from the reported errors (300 draws), refitting the polynomial continuum each draw, and computing the standard deviation of the resulting band metrics. The total uncertainty is obtained by combining the Monte Carlo (noise) and ensemble (continuum-placement) contributions in quadrature.

Laboratory experiments on CO_2 and CO_2-H_2O icy mixtures

To constrain the physical state of Europa's CO_2, we measured infrared spectra of pure CO_2 ice and CO_2:H_2O mixtures under ultra-high vacuum conditions (base pressure ~10^{-10} Torr). Ices were vapor deposited onto a gold-coated quartz crystal microbalance (QCM) cooled to 70 K. Pure CO_2 film was grown by condensing CO_2 vapor from a doser at a constant rate. Intimate CO_2-H_2O mixtures with controlled compositions were produced by co-deposition from separate CO_2 and H_2O dosers: we first established a steady CO_2 condensation rate before introducing H_2O to raise the total rate to ~50 nm minute^{-1}. Near the target thickness, the H_2O doser was closed first to ensure the CO_2 deposition rate remained within 10% of the initial value, enabling a precise calculation of CO_2 fraction in the mixture. At 70 K, CO_2 molecules could diffuse and coalesce to form crystalline clusters dispersed in water ice. Specular reflectance spectra (1 - 16 µm) were acquired with a Thermo-Nicolet is50 Fourier Transform Infrared Spectrometer at 35° incidence and at a resolution of < 1 cm^{-1}. For the CO_2:H_2O films, spectra were also measured after irradiation with 10 keV electrons using a Kimball Physics (EGG-3101) electron gun.

Water Ice Radiolysis Model

The main input to the radiolysis model is the surface irradiation fluxes for 10 keV - 100 MeV electron, protons, O^{2+} and S^{3+} ions taken from [6, 28], where simulated particles are traced through Europa's local field topology constrained by the magnetohydrodynamics model [54]. The treatment considers plasma density and

species energy distributions at Europa's orbit together with the time-variable Jovian and induced Europan fields and so resolves how electron and ion precipitation patterns shift as Jupiter's magnetodisc flaps past the moon. We adopt the time-averaged impact fluxes and use them to model the cumulative radiolytic H_2O_2 distribution in the surface ice.

The surface precipitation pattern of each species is obtained by scaling the energy distribution function, as estimated for the ambient Jovian plasma in the upstream corotation flow, by a surface latitude/longitude dependent and energy-dependent access fraction. This is the fraction of particles that, at the given energy, after flying co-rotating cycloidal trajectories that bounce north-south along Jupiter's magnetic field lines, can fly through Europa's local field topology to reach unobstructed a given latitude and longitude on the surface. The access fraction $a_i(E, \theta, \phi)$ for species i, at energy E, latitude θ and longitude ϕ, is multiplied by the upstream particle flux $f_{i0}(E)$, projected onto a surface by integrating over steradians, to obtain $f_i(E, \theta, \phi)$, the irradiation flux (e.g. $eV^{-1}cm^{-2}s^{-1}$) onto Europa's surface.

This model treats radiolysis only by ions and electrons between 10 keV and 10 MeV, the range that dominates energy deposition within the optical depth sampled by JWST, taken here as D = 50 μm. The thermal plasma < 10 keV delivers substantially more particle flux to the surface but penetrates no more than a few microns and so alters the peroxide concentration seen by JWST by <10%. Radiolytic peroxide synthesis at Enceladus was estimated in [56] using the ice radiolysis model of [26]. We adapt equations (4) and (6) of [56] to Europa to obtain peroxide creation and destruction rates in water ice. All integrations below are evaluated numerically; parenthetical quantities give dimensions in indicative units.

The peroxide creation rate in an ice at temperature T is proportional to radiolysis yield $G(T)$ (molecule eV^{-1}) times the power density $P(x)$ (eV cm^{-3} s^{-1}) deposited by all radiation species versus depth x in the ice:

$$P(x) = \sum_i \int_0^\infty f_i(E, \theta, \phi) S_i(E, x)\, dE \tag{1}$$

$$creation(x) = G(T)P(x) = G(T) \sum_i \int_0^\infty f_i(E, \theta, \phi) S_i(E, x)\, dE, \tag{2}$$

where S_i is the average stopping power (eV cm^{-1}) of particles slowed to depth x. For electrons, we neglect straggling and estimate the energy E' versus depth as $E'(E, x) = E - \int_0^x S_i(E, x')dx'$, and approximate $S_i(E, x)$ as equal to $S_i(E')$. For ions we evaluate $S_i(E, x)$ by using TRIM software [57] to estimate the average stopping power (so averaging over the straggling) for an ion at depth x. We produced a script to auto-run TRIM simulations for protons, and for O and S ions over a grid of energies, tabulating $S_i(E, x')$ across the full range of energies and depths for all three species. Creation rates average $\sim 4 - 8 \times 10^{12}$ H_2O_2 cm^{-3} s^{-1} within the top 50 μm.

The peroxide destruction rate (inverse of the H_2O_2 survival time) is the destruction cross section (cm^2) times the total particle flux over all species as a function of depth.

$$destruction(x) = \sigma_d(T) \sum_i \int_0^\infty f_i(E, \theta, \phi) F_i(E, x)\, dE, \tag{3}$$

where F_i is the fraction (0 to 1) of particles with energy E reaching depth x. The average H_2O_2 lifetime is the inverse of the destruction frequency and falls between ~2 weeks on the trailing hemisphere up to ~8 months on the leading, within the top 50 μm surficial ice. Predicted peroxide concentrations therefore peak on the leading hemisphere owing to the long survival lifetimes there; a result of the low fluxes of destructive energetic electrons on that hemisphere (Figure 4).

The steady state peroxide density n_p (cm^{-3}) as a function of depth in the ice is just the ratio of the creation rate per unit volume to the destruction rate:

$$n_p(x, \theta, \phi) = \frac{creation(x, \theta, \phi)}{destruction(x, \theta, \phi)} = \frac{G}{\sigma_d}(T) \frac{\sum_i \int_0^\infty f_i(E, \theta, \phi) S_i(E, x)\, dE}{\sum_i \int_0^\infty f_i(E, \theta, \phi) F_i(E, x)\, dE}. \tag{4}$$

The temperature dependence of $\frac{G}{\sigma_d}(T)$ was modeled in [26] on the basis of decades of laboratory data for water ice radiolysis across different projectiles and energies. We have added new electron irradiation data from [29], and the updated fit across the compiled dataset is shown in Figure S5 and the fit parameter values are discussed in the main text.

Surface temperatures versus latitude and local time follow the approach of [73], adapted from [27]. The plotted baseline peroxide distribution is referenced to T_o = 80 K (Figure S4, top panel), near the middle of the diurnally averaged range of ~49-104 K from pole to equator. Temperature effects are applied by scaling the baseline distribution by $exp(-\alpha\Delta T)$

$$\frac{G}{\sigma_d}(T) = \frac{G}{\sigma_d}(T_o)\exp(-\alpha\Delta T), \tag{5}$$

where $\Delta T = T - T_0$. We use diurnally averaged rather than instantaneous temperature, since the radiolytic time constants of weeks to months far exceed Europa's 3.55-day rotation period - too long for peroxide concentrations to track daily temperature changes.

The average relative concentration C_{avg} sensed by JWST within D = 50 microns is

$$C_{avg}(\theta,\phi) = (1/n_w)\int_0^D n_p(x,\theta,\phi)\,dx, \tag{6}$$

where n_w is the molecular density of water ice. As $n_p \ll n_w$, the conversion of water to peroxide is so minor that we approximate $n_w = 3{\times}10^{22}$ cm^{-3} as constant and unaffected by the radiolysis.

An LLM (Claude Opus 5) was used to refine the language and structure of the author-written text.

Data Availability

The JWST data used in this study are publicly available from the Mikulski Archive for Space Telescopes (MAST) at https://mast.stsci.edu/, under GTO program #1250. The data underlying all figures (including those in the supplemental information) will be deposited in public repository hosted at Zenodo or equivalent. The Global Geologic map of Europa is available at https://doi.org/10.3133/sim3513.

Code Availability

The JWST science data calibration pipeline is at https://github.com/spacetelescope/jwst. The radiolysis model is implemented within a larger toolset that couples charged particle precipitation and plume fallout, originally developed for Enceladus, and is not distributed as a standalone package. Model formulation, governing equations, and parameter values are given in full in the Methods. The complete tool set is available from the corresponding author for replication or verification purposes.

References

[1] Carr, M. H. *et al.* Evidence for a subsurface ocean on Europa. *Nature* **391**, 363–365 (1998).

[2] McKinnon, W. B., Pappalardo, R. T. & Khurana, K. K. in *Europa: Perspectives on an ocean world* (eds Pappalardo, R. T., McKinnon, W. B. & Khurana, K. K.) *Europa* 697–710 (University of Arizona Press, Tucson, 2009).

[3] Pappalardo, R. T. *et al.* Geological evidence for solid-state convection in Europa's ice shell. *Nature* **391**, 365–368 (1998).

[4] Paranicas, C., Cooper, J. F., Garrett, H. B., Johnson, R. E. & Sturner, S. J. in *Europa's radiation environment and its effects on the surface* (eds Pappalardo, R. T., McKinnon, W. B. & Khurana, K. K.) *Europa* 529–544 (University of Arizona Press, Tucson, 2009).

[5] Nordheim, T. A., Hand, K. P. & Paranicas, C. Preservation of potential biosignatures in the shallow subsurface of Europa. *Nat. Astron.* **2**, 673–679 (2018).

[6] Nordheim, T. A. *et al.* Magnetospheric ion bombardment of Europa's surface. *Planet. Sci. J.* **3**, 5 (2022).

[7] Carlson, R. W. *et al.* Hydrogen peroxide on the surface of Europa. *Science* **283**, 2062 (1999).

[8] Carlson, R. W. *et al.* in *Europa's surface composition* (eds Pappalardo, R. T., McKinnon, W. B. & Khurana, K. K.) *Europa* 283–328 (University of Arizona Press, Tucson, 2009).

[9] Anderson, J. D. *et al.* Europa's differentiated internal structure: Inferences from four Galileo encounters. *Science* **281**, 2019 (1998).

[10] Vance, S. D., Hand, K. P. & Pappalardo, R. T. Geophysical controls of chemical disequilibria in Europa. *Geophys. Res. Lett.* **43**, 4871–4879 (2016).

[11] Běhounková, M. *et al.* Tidally induced magmatic pulses on the oceanic floor of Jupiter's moon Europa. *Geophys. Res. Lett.* **48**, e90077 (2021).

[12] Hand, K. P., Chyba, C. F., Priscu, J. C., Carlson, R. W. & Nealson, K. H. in *Astrobiology and the potential for life on Europa* (eds Pappalardo, R. T., McKinnon, W. B. & Khurana, K. K.) *Europa* 589 (University of Arizona Press, Tucson, 2009).

[13] Levin, S. M. *et al.* Europa's ice thickness and subsurface structure characterized by the Juno microwave radiometer. *Nat. Astron.* **10**, 84–91 (2025).

[14] Schmidt, B. E., Blankenship, D. D., Patterson, G. W. & Schenk, P. M. Active formation of 'chaos terrain' over shallow subsurface water on Europa. *Nature* **479**, 502–505 (2011).

[15] Nimmo, F. & Manga, M. Causes, characteristics and consequences of convective diapirism on Europa. *Geophys. Res. Lett.* **29**, 2109 (2002).

[16] Bierhaus, E. B., Zahnle, K. & Chapman, C. R. in *Europa's crater distributions and surface ages* (eds Pappalardo, R. T., McKinnon, W. B. & Khurana, K. K.) *Europa* 161 (University of Arizona Press, Tucson, 2009).

[17] Roth, L. *et al.* Transient water vapor at Europa's south pole. *Science* **343**, 171–174 (2014).

[18] Kattenhorn, S. A. & Prockter, L. M. Evidence for subduction in the ice shell of Europa. *Nat. Geosci.* **7**, 762–767 (2014).

[19] Villanueva, G. L. *et al.* Endogenous CO_2 ice mixture on the surface of Europa and no detection of plume activity. *Science* **381**, 1305–1308 (2023).

[20] Trumbo, S. K. & Brown, M. E. The distribution of CO_2 on Europa indicates an internal source of carbon. *Science* **381**, 1308–1311 (2023).

[21] Trumbo, S. K., Brown, M. E. & Hand, K. P. H_2O_2 within chaos terrain on Europaś leading hemisphere. *Astron. J.* **158**, 127 (2019).

[22] Wu, P., Trumbo, S. K., Brown, M. E. & de Kleer, K. Europa's H_2O_2: Temperature insensitivity and a correlation with CO_2. *Planet. Sci. J.* **5**, 220 (2024).

[23] Raut, U. *et al.* Can endogenic CO_2 inflate radiolytic H_2O_2 in Europa's chaos? (2024). EGU General Assembly 2024, EGU24-6579.

[24] Loeffler, M. J., Raut, U., Vidal, R. A., Baragiola, R. A. & Carlson, R. W. Synthesis of hydrogen peroxide in water ice by ion irradiation. *Icarus* **180**, 265–273 (2006).

[25] Hand, K. P. & Carlson, R. W. H_2O_2 production by high-energy electrons on icy satellites as a function of surface temperature and electron flux. *Icarus* **215**, 226–233 (2011).

[26] Teolis, B. D., Plainaki, C., Cassidy, T. A. & Raut, U. Water ice radiolytic O_2, H_2, and H_2O_2 yields for any projectile species, energy, or temperature: A model for icy astrophysical bodies. *J. Geophys. Res.*

Planets **122**, 1996–2012 (2017).

[27] Spencer, J. R., Tamppari, L. K., Martin, T. Z. & Travis, L. D. Temperatures on Europa from Galileo photopolarimeter-radiometer: Nighttime thermal anomalies. *Science* **284**, 1514 (1999).

[28] Nordheim, T. A. *et al.* Magnetospheric charged particle irradiation of Jupiter's moon Europa. *Planet. Sci. J.* **XX** (2026).

[29] Mamo, B. D. *et al.* Laboratory investigation of CO_2-driven enhancement of radiolytic H_2O_2 on Europa and other icy moons. *Planet. Sci. J.* **6**, 170 (2025).

[30] Böker, T. *et al.* In-orbit performance of the near-infrared spectrograph NIRSpec on the James Webb Space Telescope. *Publ. Astron. Soc. Pac.* **135**, 038001 (2023).

[31] Villanueva, G. L., Smith, M. D., Protopapa, S., Faggi, S. & Mandell, A. M. Planetary Spectrum Generator: An accurate online radiative transfer suite for atmospheres, comets, small bodies and exoplanets. *J. Quant. Spectrosc. Radiat. Transf.* **217**, 86–104 (2018).

[32] Hase, F., Wallace, L., McLeod, S. D., Harrison, J. J. & Bernath, P. F. The ACE-FTS atlas of the infrared solar spectrum. *J. Quant. Spectrosc. Radiat. Transf.* **111**, 521–528 (2010).

[33] Protopapa, S. *et al.* Detection of carbon dioxide and hydrogen peroxide on the stratified surface of Charon with JWST. *Nat. Commun.* **15**, 8247 (2024).

[34] Quirico, E. & Schmitt, B. Near-infrared spectroscopy of simple hydrocarbons and carbon oxides diluted in solid N2 and as pure ices: Implications for Triton and Pluto. *Icarus* **127**, 354–378 (1997).

[35] Quirico, E. & Schmitt, B. Near-IR optical constants of crystalline CO_2 ice at 179 k completed with 28 k data. 1 spectrum. SSHADE/GhoSST (OSUG Data Center) (2018).

[36] Öberg, K. I., Fayolle, E. C., Cuppen, H. M., van Dishoeck, E. F. & Linnartz, H. Quantification of segregation dynamics in ice mixtures. *Astron. Astrophys.* **505**, 183–194 (2009).

[37] He, J., Emtiaz, S. M. & Vidali, G. Diffusion and clustering of carbon dioxide on non-porous amorphous solid water. *Astrophys. J.* **837**, 65 (2017).

[38] Raut, U. & Baragiola, R. A. Sputtering and molecular synthesis induced by 100 kev protons in condensed CO_2 and relevance to the outer Solar System. *Astrophys. J.* **772**, 53 (2013).

[39] Oancea, A. *et al.* Laboratory infrared reflection spectrum of carbon dioxide clathrate hydrates for astrophysical remote sensing applications. *Icarus* **221**, 900–910 (2012).

[40] Hibbitts, C. A., Pappalardo, R. T., Hansen, G. B. & McCord, T. B. Carbon dioxide on Ganymede. *J. Geophys. Res. Planets* **108**, 5036 (2003).

[41] Bockelée-Morvan, D. *et al.* Composition and thermal properties of Ganymede's surface from JWST/NIRSpec and MIRI observations. *Astron. Astrophys.* **681**, A27 (2024).

[42] Cartwright, R. J. *et al.* Revealing Callisto's carbon-rich surface and CO_2 atmosphere with JWST. *Planet. Sci. J.* **5**, 60 (2024).

[43] Cartwright, R. J. *et al.* JWST reveals spectral tracers of recent surface modification on Europa. *Planet. Sci. J.* **6**, 125 (2025).

[44] Leonard, E. J., Patthoff, D. A. & Senske, D. A. Global geologic map of Europa. Scientific Investigations Map 3513, U.S. Geological Survey, Reston, VA (2024).

[45] Hansen, G. B. & McCord, T. B. Amorphous and crystalline ice on the Galilean satellites: A balance between thermal and radiolytic processes. *J. Geophys. Res. Planets* **109**, E01012 (2004).

[46] Dalton, J. B., III, Shirley, J. H. & Kamp, L. W. Europa's icy bright plains and dark linea: Exogenic and endogenic contributions to composition and surface properties. *J. Geophys. Res. Planets* **117**, E03003 (2012).

[47] Becker, T. M. *et al.* Exploring the composition of Europa with the upcoming Europa clipper mission. *Space Sci. Rev.* **220**, 49 (2024).

[48] Shirley, J. H., Dalton, J. B., Prockter, L. M. & Kamp, L. W. Europa's ridged plains and smooth low albedo plains: Distinctive compositions and compositional gradients at the leading side-trailing side boundary. *Icarus* **210**, 358–384 (2010).

[49] Gerakines, P. A. & Hudson, R. L. A modified algorithm and open-source computational package for the determination of infrared optical constants relevant to astrophysics. *Astrophys. J.* **901**, 52 (2020).

[50] Hand, K. P., Carlson, R. W. & Chyba, C. F. Energy, chemical disequilibrium, and geological constraints on Europa. *Astrobiology* **7**, 1006–1022 (2007).

[51] Moore, M. H. & Hudson, R. L. IR detection of H_2O_2 at 80 k in ion-irradiated laboratory ices relevant to Europa. *Icarus* **145**, 282–288 (2000).

[52] Breer, B. R., Liuzzo, L., Arnold, H., Andersson, P. N. & Simon, S. Energetic ion dynamics in the perturbed electromagnetic fields near Europa. *J. Geophys. Res. Space Phys.* **124**, 7592–7613 (2019).

[53] Addison, P., Liuzzo, L., Arnold, H. & Simon, S. Influence of Europa's time varying electromagnetic environment on magnetospheric ion precipitation and surface weathering. *J. Geophys. Res. Space Phys.* **126**, e29087 (2021).

[54] Harris, C. D. K. *et al.* Multi fluid MHD simulations of Europa's plasma interaction under different magnetospheric conditions. *J. Geophys. Res. Space Phys.* **126**, e28888 (2021).

[55] Cassidy, T. A. *et al.* Magnetospheric ion sputtering and water ice grain size at Europa. *Planet. Space Sci.* **77**, 64–73 (2013).

[56] Ray, C. *et al.* Oxidation processes diversify the metabolic menu on Enceladus. *Icarus* **364**, 114248 (2021).

[57] Ziegler, J. F. & Biersack, J. P. in *The stopping and range of ions in matter* (ed.Bromley, D. A.) *Treatise on Heavy-Ion Science*, Vol. 6 93–129 (Springer US, Boston, MA, 1985).

[58] Loeffler, M. J., Teolis, B. D. & Baragiola, R. A. Decomposition of solid amorphous hydrogen peroxide by ion irradiation. *J. Chem. Phys.* **124**, 104702 (2006).

[59] Paranicas, C., Carlson, R. W. & Johnson, R. E. Electron bombardment of Europa. *Geophys. Res. Lett.* **28**, 673–676 (2001).

[60] Hand, K. P. & Brown, M. E. Keck II observations of hemispherical differences in H_2O_2 on Europa. *Astrophys. J.* **766**, L21 (2013).

[61] Grundy, W. M. *et al.* New horizons mapping of Europa and Ganymede. *Science* **318**, 234 (2007).

[62] Ligier, N., Poulet, F., Carter, J., Brunetto, R. & Gourgeot, F. VLT/SINFONI observations of Europa: New insights into the surface composition. *Astron. J.* **151**, 163 (2016).

[63] Trumbo, S. K., Brown, M. E. & Hand, K. P. Sodium chloride on the surface of Europa. *Sci. Adv.* **5**, aaw7123 (2019).

[64] Hesse, M. A., Jordan, J. S., Vance, S. D. & Oza, A. V. Downward oxidant transport through Europa's ice shell by density-driven brine percolation. *Geophys. Res. Lett.* **49**, e2021GL095416 (2022).

[65] Byrne, P. K. *et al.* Little to no active faulting likely at Europa's seafloor today. *Nat. Commun.* **17**, 4 (2026).

[66] Green, A. P., Elder, C. M., Bland, M. T., Tackley, P. J. & Byrne, P. K. No magmatic driving force for Europan sea-floor volcanism. *Nat. Astron.* **9**, 640–649 (2025).

[67] DelloRusso, N., Khanna, R. K. & Moore, M. H. Identification and yield of carbonic acid and formaldehyde in irradiated ices. *J. Geophys. Res. Planets* **98**, 5505–5510 (1993).

[68] Luna, R. *et al.* Densities, infrared band strengths, and optical constants of solid methanol. *Astron. Astrophys.* **617**, A116 (2018).

[69] Protopapa, S. *et al.* JWST detection of hydrocarbon ices and methane gas on Makemake. *Astrophys. J.* **991**, L34 (2025).

[70] Bushouse, H. *et al.* JWST calibration pipeline. Zenodo (2024).

[71] Rauscher, B. J. NSClean: An algorithm for removing correlated noise from JWST NIRSpec images. *Publ. Astron. Soc. Pac.* **136**, 015001 (2024).

[72] Acton, C. H. Ancillary data services of NASA's navigation and ancillary information facility. *Planet. Space Sci.* **44**, 65–70 (1996).

[73] Teolis, B. D., Wyrick, D. Y., Bouquet, A., Magee, B. A. & Waite, J. H. Plume and surface feature structure and compositional effects on Europa's global exosphere: Preliminary Europa mission predictions. *Icarus* **284**, 18–29 (2017).

Funding. This work was supported by the NASA Solar System Workings program through grant 80NSSC24K0657 (UR, BT, SP, TP - partial support), the NASA Future Investigators in NASA Earth and Space Science and Technology (FINESST) program through grant 80NSSC23K1386 (BM), and the NASA Europa Clipper ICONS program RSA 1711180 (TE). UR, BT, BM, JAK and KDR were partially supported by the Europa Clipper mission under contract 80NM0018D0004.

Author Contributions. **UR:** Conceptualization, Methodology, Formal analysis, Investigation, Supervision, Project administration, Funding acquisition, Visualization, Writing – original draft, Writing – review & editing. **BT:** Methodology, Investigation, Software, Formal analysis, Supervision, Writing – original draft, Writing – review & editing. **TN:** Methodology, Investigation, Formal Analysis, Resources, Writing – review & editing. **SP:** Data curation, Software, Formal analysis, Investigation, Writing – review & editing. **BM:** Investigation, Formal analysis, Writing – review & editing. **TE:** Investigation, Formal analysis, Writing – review & editing. **IW:** Data curation, Writing – review & editing. **JAK:** Data curation, Software, Writing – review & editing. **KDR:** Funding acquisition, Writing – review & editing. **RJC:** Writing – review & editing. **TP:** Investigation, Writing – review & editing. **GV:** Writing – review & editing. **SDV:** Writing – review & editing.

Correspondence and request for materials should be addressed to Ujjwal Raut.

Competing interests. The authors declare no competing interests.

Supplementary Materials for

Ocean-sourced CO_2 Boosts Radiolytic Oxidants at Europa's Chaos

U. Raut et al.

The file includes:

Figures S1–S5.

References

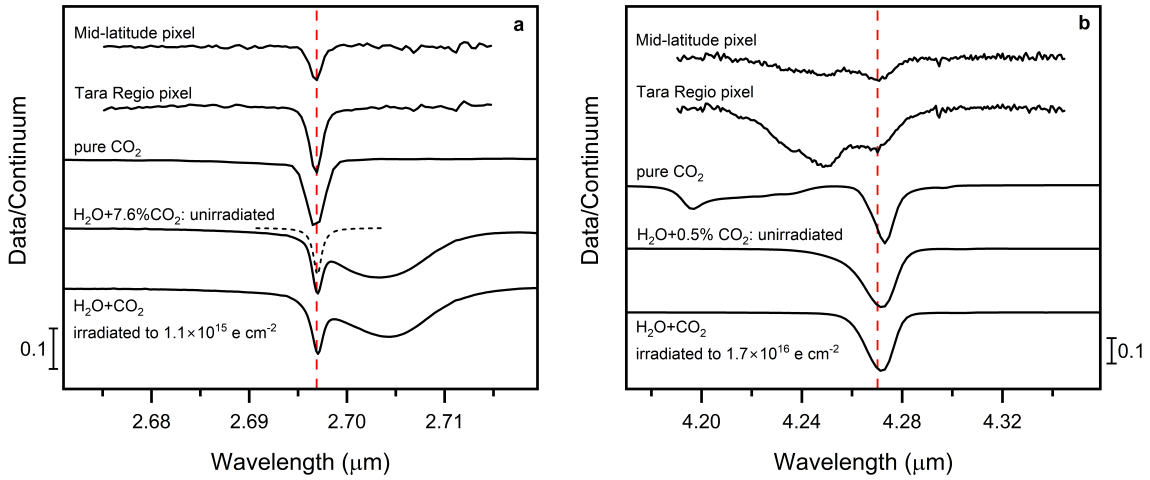


Fig. S1 | Physical state of carbon dioxide on the surface of Europa. a) Continuum-corrected Europa spectra from a Tara Regio and a mid-latitude pixel, showing the narrow $\nu_1 + \nu_3$ CO_2 band at 2.697 μm (red vertical dashed line), compared with laboratory spectra of pure crystalline CO_2 ice and CO_2 diluted in H_2O ice (pristine and irradiated with 10 keV electrons to a fluence of 1.1×10^{15} cm^{-2}) at 70 K. The laboratory spectra have been scaled to match the band depth of the Tara Regio spectrum. Europa's $\nu_1 + \nu_3$ band agrees with the pure crystalline CO_2 ice peak position (within 0.5 nm), as do the dilute mixtures, pre- and post-irradiation. The broad overlapping band near 2.704 μm in the laboratory spectra of mixed H_2O-CO_2 ice is attributed to disordered CO_2 molecules interacting with the water ice matrix [1]. The dashed spectra is the deconvolved Lorentzian component, distinct from the overlapping disordered-CO_2 absorption. This sharp 2.697 μm component is the spectral signature of crystalline CO_2 [2], embedded within the water ice matrix. CO_2 molecules, even though initially deposited into an intimately mixed state, can diffuse and coalesce into crystalline clusters at 70 K [1,3]. b) As in a, but for the fundamental ν_3 CO_2 band. Europa's ν_3 band differs starkly from the laboratory spectra shown here: it is a doublet, with components near 4.25 and 4.27 μm, whereas pure crystalline CO_2 as well as H_2O ice containing trace amounts of CO_2- pristine and irradiated alike, present only the 4.27 μm band. The missing 4.25 μm band dominates the Tara Regio spectra. It may reflect the need for additional components like brine or organics in the laboratory ices, though recent study showed CO_2 in pores or cracks in the ice may produce the 4.25 μm absorption [4]. Europa's 4.27 μm component, in contrast, agree with the laboratory bands: its position agree to within 3 nm and lies < 2 nm blueward of the pure crystalline CO_2 ice. The two laboratory cases are themselves nearly co-incident such that their peak position alone is not diagnostic of Europa's CO_2 – whether it is present as pure crystalline deposit or dispersed in water ice. Taken together, the two panels indicate that CO_2 on Europa is likely present as crystalline clusters, hosted within a water ice matrix and such confinements enable the stability of solid CO_2 at warmer surfaces on Europa exceeding 100 K. The feature at 4.20 μm in the pure CO_2 spectrum is a longitudinal optical phonon mode [5]. Spectra are vertically offset for clarity.

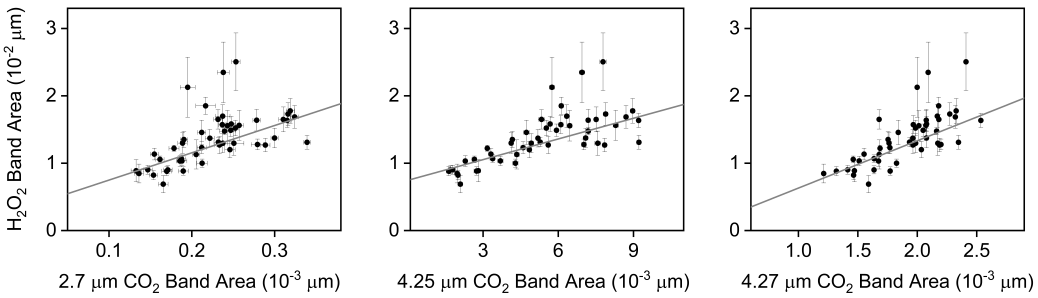


Fig. S2 | Linked CO_2-H_2O_2 in Europa's chaos ice. Strong positive correlation between Europa's 3.5 μm H_2O_2 and CO_2 band areas as revealed by three linear fits with Pearson's coefficient increasing from 0.73, 0.78 and 0.82 from left to right. This correlation suggests CO_2 may influence radiolytic peroxide synthesis which was confirmed in the laboratory (Figure 3). The CO_2-driven boost factor was used to estimate the steady-state H_2O_2 concentration at the chaos terrains and across Europa's leading hemisphere.

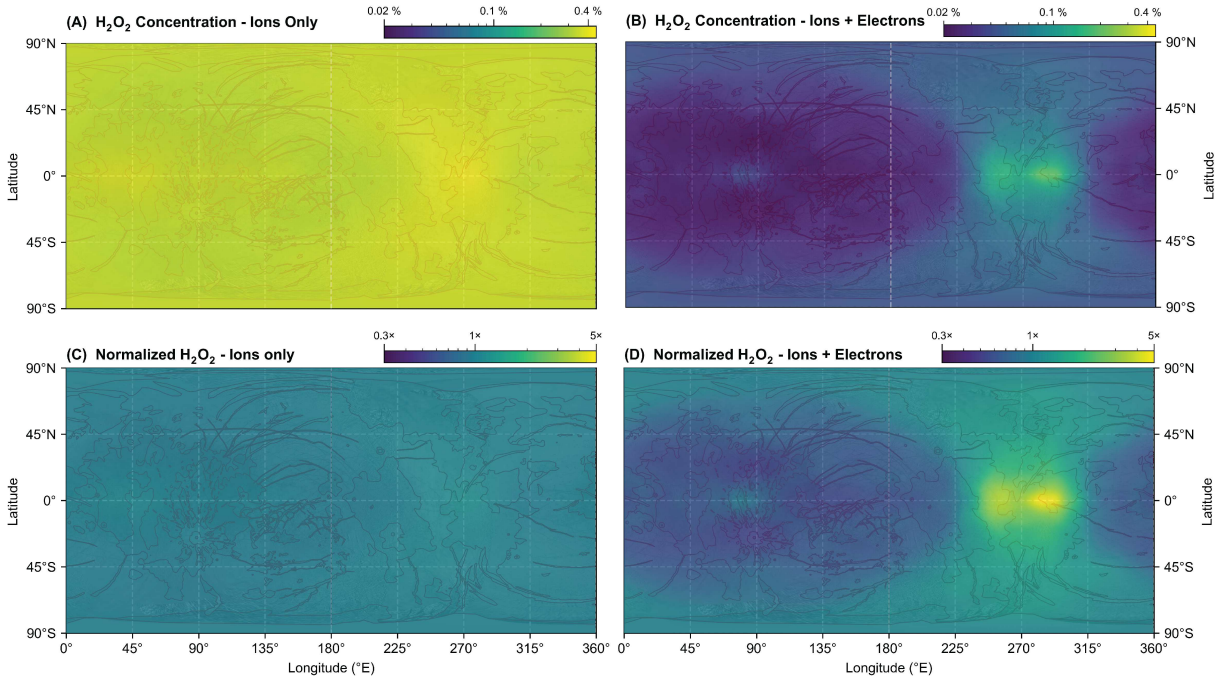


Fig. S3 | Energetic electrons – primary destroyer of Europa's peroxide. The predicted near-uniform peroxide concentration from radiolysis of pure water ice by energetic ions only (H^+, O^{2+}, S^{3+} across 10 keV- 100 MeV) at 80 K, averaged over the 50 μm depth (panel A). Including electrons over the same energy range (panel B) drastically alters the steady-state H_2O_2 concentration, with trailing side heavily depleted and the region in the vicinity of the leading apex showing elevated levels of peroxide. Away from the leading equatorial region, the electron fluxes are sufficiently high to effectively destroy peroxide produced primarily by heavy ions within the optical sensing depth, assumed 50 μm. The peroxide concentration presented in panels A and B are normalized by the respective global averages in panel C (ions only) and D (all species) to further emphasize the small deviation from the mean value across the global surface in the case of ions-only radiolysis. By contrast, the deviation from the mean is significantly larger in panel D, confirming the energetic electrons, owing to their destructive nature, are largely responsible for the asymmetry in Europa's peroxide distribution.

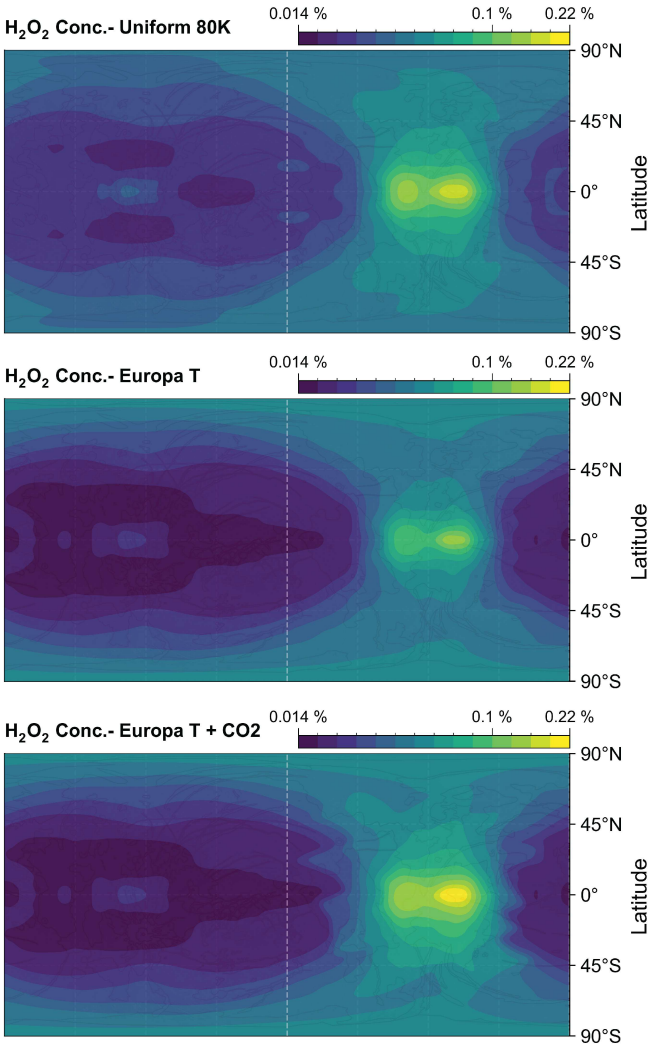


Fig. S4 | Thermal suppression and the CO_2-driven boost in H_2O_2 yields. Predicted peroxide distributions within the 50 μm optical skin for three cases. With the assumption of pure water ice at a uniform 80 K temperature (top), concentrations peak at the leading hemisphere apex, owing to a dearth of energetic electron flux at that location capable of efficiently destroying peroxide through the skin depth. Equilibrium peroxide concentrations decline with ice temperature according to laboratory experiments [6], and therefore the addition of Europa's diurnally averaged (latitude-dependent) surface temperature to the model suppresses the equatorial concentrations (middle panel). However, as we show here, the thermal suppression is counteracted by adding CO_2 to the ice (bottom). The three maps share a logarithmic color scale (0.014 - 0.22 % H_2O_2) divided into 14 equal-ratio bands.

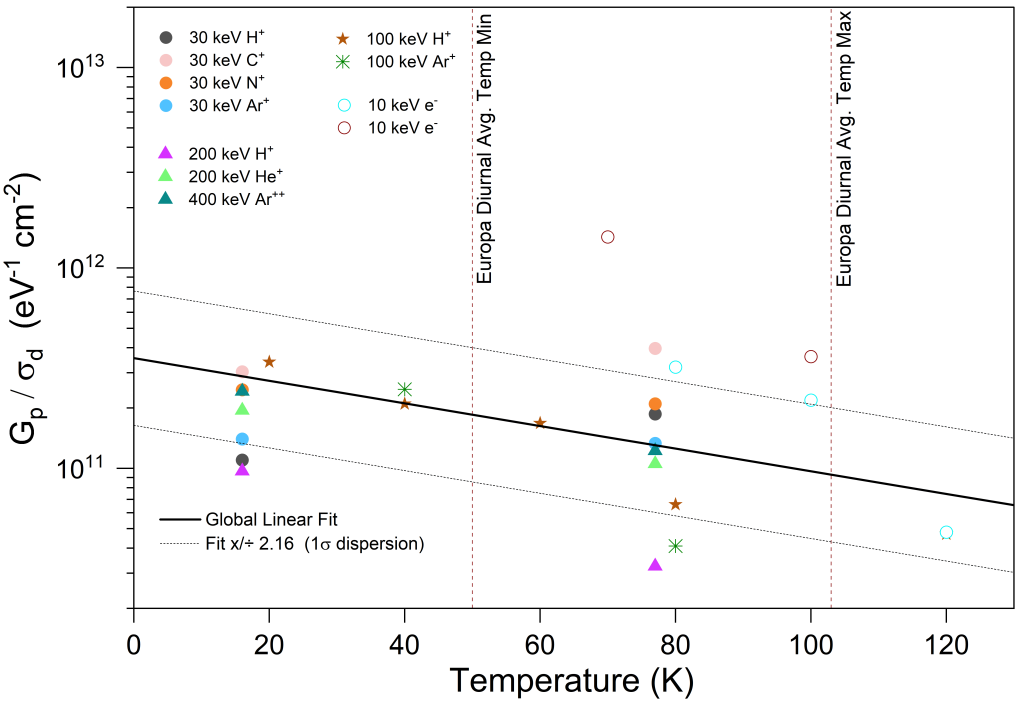


Fig. S5 | Exponential decline of G_p/σ_d with ice temperature. G_p/σ_d values are obtained from the fluence dependence data of H_2O_2 production in pure-ice radiolysis experiments, previously compiled in [7]. 30 keV H^+, C^+, N^+, Ar^+ ions from [8]; 200 keV H^+, He^+ and 400 keV Ar^{2+} from [9]; 100 keV H^+ and Ar^+ from [6]; 10 keV electrons from [10]. We added new 10 keV electron irradiation data from [11]. The datasets are treated as 11 projectile-energy series (as indicated in the legend) which were fit jointly with a common-slope model, $\ln(G_p/\sigma_d) = \ln(G_p/\sigma_d)_o - \alpha T$. The fit, indicated by the solid black line, yields a single $\alpha = 0.013$ (± 0.0041) K^{-1} and intercept $(G_p/\sigma_d)_o = 3.55 \times 10^{11}$ eV^{-1} cm^{-2}, the geometric mean of the series intercepts. Dotted lines mark the fit multiplied and divided by 2.16, the 1σ dispersion about it, with α held constant such that bounds appear parallel to the fit. Vertical dashed lines bracket Europa's diurnally-averaged surface temperature. The equilibrium H_2O_2 abundance at a given temperature is $G_p/\sigma_d(T)$ multiplied by the flux-weighted stopping cross section S.

References

1. He, J., Emtiaz, S., Boogert, A. & Vidali, G. The $^{12}CO_2$ and $^{13}CO_2$ Absorption Bands as Tracers of the Thermal History of Interstellar Icy Grain Mantles. *ApJ* **869**, 41 (2018).

2. Isokoski, K., Poteet, C. A. & Linnartz, H. Highly resolved infrared spectra of pure CO_2 ice (15–75 K). *A&A* **555**, A85 (2013).

3. Öberg, K. I., Fayolle, E. C., Cuppen, H. M., van Dishoeck, E. F. & Linnartz, H. Quantification of segregation dynamics in ice mixtures. *Astronomy and Astrophysics* **505**, 183–194 (2009).

4. Schiltz, L. et al. Characterization of carbon dioxide on Ganymede and Europa supported by experiments: Effects of temperature, porosity, and mixing with water. *A&A* **688**, A155 (2024).

5. Cooke, I. R., Fayolle, E. C. & Öberg, K. I. CO_2 Infrared Phonon Modes in Interstellar Ice Mixtures. *The Astrophysical Journal* **832**, 5 (2016).

6. Loeffler, M. J., Raut, U., Vidal, R. A., Baragiola, R. A. & Carlson, R. W. Synthesis of hydrogen peroxide in water ice by ion irradiation. *Icarus* **180**, 265–273 (2006).

7. Teolis, B. D., Plainaki, C., Cassidy, T. A. & Raut, U. Water Ice Radiolytic O_2, H_2, and H_2O_2 Yields for Any Projectile Species, Energy, or Temperature: A Model for Icy Astrophysical Bodies. *Journal of Geophysical Research (Planets)* **122**, 1996–2012 (2017).

8. Gomis, O., Satorre, M. A., Strazzulla, G. & Leto, G. Hydrogen peroxide formation by ion implantation in water ice and its relevance to the Galilean satellites. *Planetary and Space Science* **52**, 371–378 (2004).

9. Gomis, O., Leto, G. & Strazzulla, G. Hydrogen peroxide production by ion irradiation of thin water ice films. *Astronomy and Astrophysics* **420**, 405–410 (2004).

10. Hand, K. P. & Carlson, R. W. H_2O_2 production by high-energy electrons on icy satellites as a function of surface temperature and electron flux. *Icarus* **215**, 226–233 (2011).

11. Mamo, B. D. et al. Laboratory Investigation of CO_2-driven Enhancement of Radiolytic H_2O_2 on Europa and Other Icy Moons. *The Planetary Science Journal* **6**, 170 (2025).